Supported metal catalysts with single-atom promoters via reductive atom trapping

Dong Jiang,[1] Hien N. Pham,[2] Yixiao Li,[1] Yubing Lu,[3] Wenda Hu,[1] Gang Wan,[4] Chaochao Dun,[3] Junrui Li,[1] Carlos E. García-Vargas,[1] Yipeng Sun,[5] Anthony Savoy,[1] Weixin Huang,[1] Rui Zhang,[1] Andrew T. DeLaRiva,[2] R. Soyoung Kim,[3] Xiang Li,[6] Jeffrey J. Urban,[3] Junko Yano,[3] Kelly Shelly,[7] Chengjun Sun,[7] Konstantin Khivantsev,[8] Christopher J. Tassone,[6] Jianzhi Hu,[8] Janos Szanyi,[8] Abhaya K. Datye,[2]* Yong Wang[1,8]*

Affiliations:

[1] The Gene and Linda Voiland School of Chemical Engineering and Bioengineering, Washington State University, Pullman, WA 99164, USA.

[2] Department of Chemical and Biological Engineering and Center for Micro-Engineered Materials, University of New Mexico, Albuquerque, NM 87131, USA.

[3] Lawrence Berkeley National Laboratory, Berkeley, CA 94720, USA.

[4] Department of Mechanical Engineering, Stanford University, Stanford, CA 94305

[5] Environmental Catalysis, BASF Corporation, Iselin, NJ, USA

[6] SLAC National Accelerator Laboratory, Menlo Park, CA 94025, USA.

[7] Advanced Photon Source, Argonne National Laboratory, Lemont, IL 60439, USA.

[8] Institute for Integrated Catalysis, Pacific Northwest National Laboratory, Richland, WA 99354, USA.

*Corresponding author: yong.wang@pnnl.gov, datye@unm.edu

Abstract: Nanosized cerium oxide (CeO_2) has been extensively used as an oxygen storage component in automotive emission control systems. However, possible involvement of atomically dispersed cerium (Ce) has not been explored. Here, we demonstrate the controllable transformation of CeO_2 nanoparticles into isolated Ce_1 cations on the surface of gamma-type alumina (γ-Al_2O_3) via reductive atom trapping, achieving over half-monolayer coverage. Supported single-atom rhodium (Rh_1) surrounded by dispersed Ce_1 shows superior performance to Rh_1 on bare Al_2O_3 or crystalline CeO_2 in catalyzing NO reduction, exhibiting a striking one-order-of-magnitude increase in turnover frequency. Dispersed Ce_1 also exhibits greatly enhanced oxygen transfer capability and introduced a modified reaction mechanism that involves adjacent Rh_1-Ce_1 dual-sites, resulting in a greatly decreased activation barrier (96 vs. 192 kJ/mol). The understanding of reductive atom trapping of Ce_1 as well as its structure-property relationships obtained in this work could be implemented in the rational design of Ce_1-promoted catalysts for many other applications. Benefiting from the greatly enhanced OSC, activity enhancements are also seen with Ce_1-promoted platinum nanoparticles for the oxidation of CO and hydrocarbons. Additionally, dispersing Ce_1 on Al_2O_3 results in modified surface properties, which could be further utilized to explore the field of acid-base catalysis.

Ceria (CeO_2) with a face-centered cubic fluorite structure is technologically important due to its wide applications in catalysis, gas sensors, ceramic fuel cells, water splitting, and many others (*1, 2*). As a structural and electronic promoter, nanosized ceria has attracted intense interest in catalyzing various thermo-, photo-, and electro- chemical reactions (*3-5*). Such versatility originates from facile transformations of cerium oxidation state between Ce^{4+} and Ce^{3+} in redox environments, accompanied by the release, storage, and transport of lattice oxygen. Great progress has been made in tailoring the properties of ceria via different strategies, including heteroatom doping, facet regulating, and defect engineering (*6-9*). Despite great success in understanding crystalline ceria, knowledge of spatially isolated cerium atoms in heterogeneous catalysis is very limited, in contrast to homogeneous reactions over cerium complexes (*10, 11*).

With advances in material synthesis and characterization on an atomic scale, single-atom catalysts (SACs) with isolated metal centers have attracted great interest in bridging the material gap between homogeneous and heterogeneous catalysts (*12-14*). Atomically dispersed Ce_1 has been occasionally observed on oxides and was suspected to influence catalytic properties (*15-19*). For example, highly dispersed CeO_x species were deposited onto Al_2O_3 via a pulsed arc-plasma process (*15*). Recently, we also observed increased populations of dispersed CeO_x in commercial CeO_2-Al_2O_3 oxides after running emission control reactions (*20*). The loading of Ce_1 is typically low (< 1 wt %), beyond which crystalline CeO_2 nanoparticles (NPs) form (*15, 17, 19*). Moreover, the location of dispersed Ce_1 and its interaction with the support and active centers are largely unknown. Due to the lack of precise control on Ce_1 dispersion over a wide range of loadings, key information is missing in linking its structure and catalytic properties.

Here, we present the controllable transformation of ceria NPs into isolated cerium cations on the surface of non-reducible oxides like Al_2O_3 and SiO_2. Over half-monolayer Ce_1 coverage on Al_2O_3 can be achieved with ~ 10 wt % CeO_2 loading via reductive atom trapping. The dispersed Ce_1 cations are anchored by surface penta- and octa-coordinated Al sites and are thermally stable in air up to 500 °C. With precise control of CeO_2 dispersion, single-atom $Rh_1/Ce_1/Al_2O_3$ catalysts with well-defined hierarchical structures are constructed for NO reduction by CO. Dispersed Ce_1 on Al_2O_3 exhibits much superior oxygen transfer capability compared to crystalline CeO_2. Ce_1 neighboring Rh_1 substantially modifies the reaction mechanism between NO and CO, rendering a greatly lowered activation energy barrier and greatly enhanced NO reduction activity.

Ceria/alumina mixed oxides have been widely employed in automotive emissions control, combing the outstanding redox property of CeO_2 as a promoter and the superior poisoning and sintering resistance of Al_2O_3 as a support (*21*). In this work, different amounts of cerium (III) nitrate (0-10 wt % CeO_2 basis) were deposited on the surface of a commercial γ-Al_2O_3 (~ 130 m^2/g) via incipient wetness impregnation followed by calcination in air at 800 °C. As-obtained CeO_2/Al_2O_3 is termed as CAx with x indicating the content (wt %) of CeO_2. Well defined X-ray diffraction peaks from crystalline CeO_2 with a cubic fluorite structure were evident once CeO_2 loading was > 2 wt % (fig. S1). Absence of CeO_2 diffraction peaks in CA02 could be due to the low CeO_2 content and the high dispersion. Introduction of CeO_2 with a high sintering tendency resulted in the slightly decreased surface areas of air-calcined CAx (fig. S2), e.g., 117 m^2/g for CA10 compared to 133 m^2/g for pristine γ-Al_2O_3.

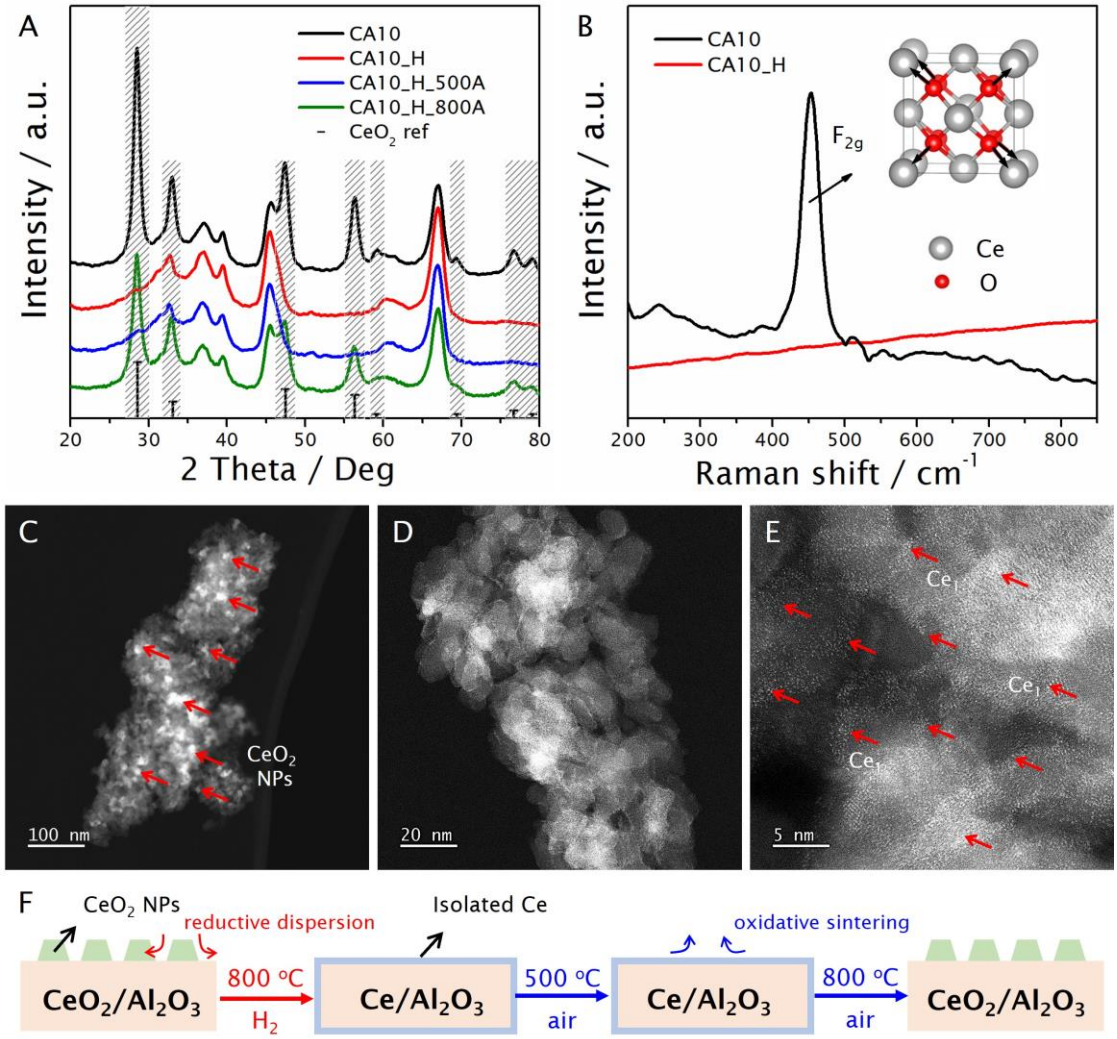

Fig. 1. Reductive dispersion of ceria NPs into isolated cerium atoms on γ-Al_2O_3. (**A**) X-ray diffraction (XRD) patterns of the 10 wt % CeO_2/Al_2O_3 after calcination in air (CA10), high-temperature (800 °C) reduction in 10 % H_2 (_H), and subsequent air calcination at 500 °C (_500A) and 800 °C (_800A). (**B**) Raman (532 nm) spectra of CA10 and CA10_H. Inset is the F_{2g} vibration mode of cubic fluorite structure. (**C**) AC-STEM image of CA10 showing the presence of CeO_2 NPs. (**D**) - (**E**) AC-STEM images of CA10_H showing the absence of CeO_2 NPs and abundant presence of isolated Ce_1. (**F**) Schematic of the reductive dispersion and oxidative sintering of Ce_1.

Interestingly, all CeO_2 diffraction peaks in CAx (e.g., CA10) diminished after being reduced in 10 % H_2 at 800 °C (CA10_H) while the crystalline structure of γ-Al_2O_3 remained unchanged (Fig. 1A). This suggests either CeO_2 dispersion into dispersed Ce_1 or the amorphization of NPs, the latter being excluded since no NPs were detected via imaging (shown later). The reductive dispersion of CeO_2 on Al_2O_3 was also suggested by the disappearance of the Raman active F_{2g} mode in CA10_H, originating from a symmetric vibration of tetrahedrally-coordinated oxygen ions (Fig. 1B). A similar Raman change was once reported by Shyu et al., attributing it to the formation of $CeAlO_3$ phase (*22*), which we did not detect via XRD/TEM. The structural changes were further confirmed by aberration-corrected scanning transmission electron microscopy (AC-STEM). As shown, CA10 mostly contains CeO_2 NPs on Al_2O_3 (Fig. 1C), although small amounts of dispersed Ce_1 (< 1 wt %) were also occasionally observed (fig. S3), consistent with previous

reports on Al_2O_3 and TiO_2 (*17, 18*). Notably, only isolated Ce_1 was observed after H_2 reduction, densely covering γ-Al_2O_3 (Figs. 1D and 1E).

Based on these characterization results, we can conclude that there happened the reductive dispersion of CeO_2, driven by high-temperature CeO_2 amorphization in a reducing atmosphere, followed by spreading and anchoring of reduced Ce_1 species on Al_2O_3 (Fig. 1F). Sublimation of nanosized CeO_2 has been noticed via TEM upon prolonged exposure to a focused electron beam or under vacuum at high temperatures (*23*). Dispersed Ce_1 is stabilized by the support to a great extent and doesn't sinter in air up to 500 ºC (Fig. 1A). The as-formed Ce_1/Al_2O_3 structure differs from crystalline $CeAlO_3$ polymorphs generated via solid-state reaction between CeO_2 and Al_2O_3 at much higher temperatures, e.g., > 900 ºC (*24*). The upper limit for CeO_2 dispersion was found to be ~ 10 wt % (i.e., CA10) for the Al_2O_3 used in this study since crystalline CeO_2 was detected by XRD beyond this threshold (fig. S4). This corresponds to over half-monolayer coverage of Al_2O_3, giving a surface density of ~ 3.5 Ce/nm^2 (fig. S5) (*16*). Such reductive dispersion of Ce_1 was also observed on other non-reducible supports such as SiO_2 (fig. S6). An intimate contact between CeO_2 and Al_2O_3 is necessary for achieving the Ce_1 dispersion since it does not happen through vapor phase for a physical mixture of CeO_2 and Al_2O_3 (fig. S7).

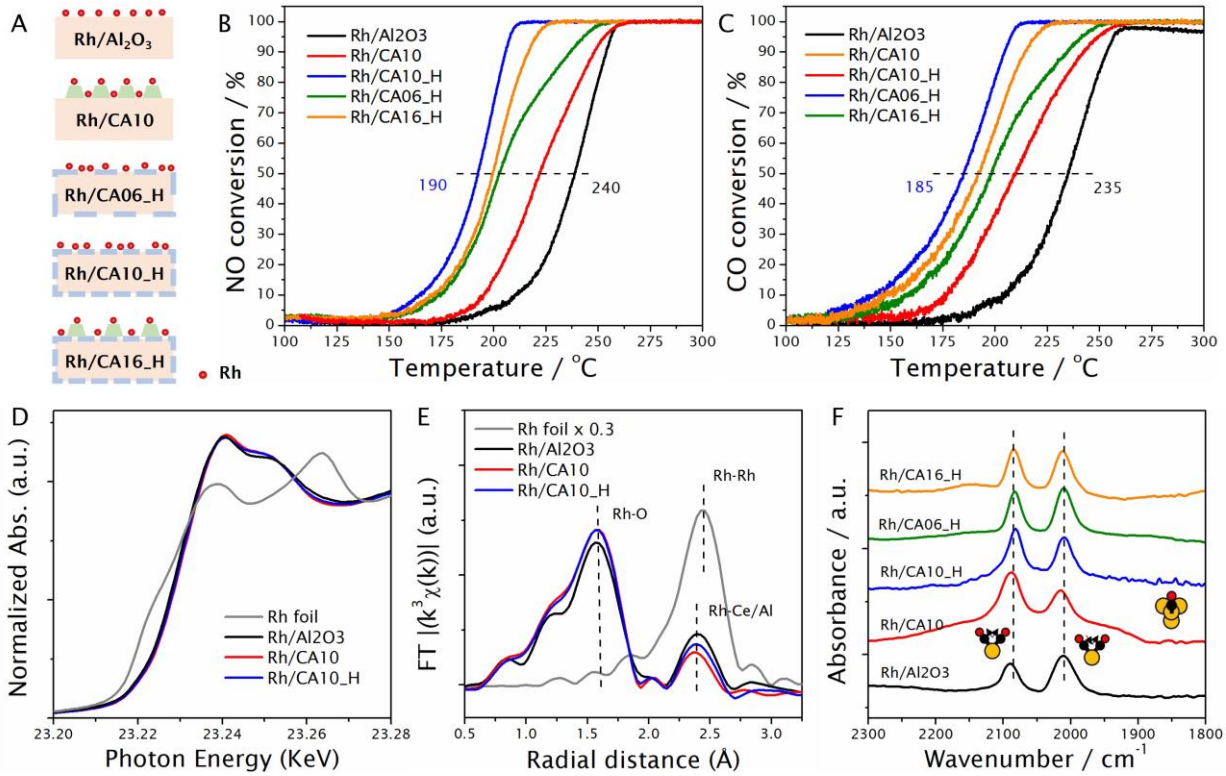

Fig. 2. Performance and spectroscopic characterization of Rh-based catalysts. (**A**) Schematic of Rh (0.1 wt %) on different supports, including Al_2O_3, CAx, CAx_H, and CeO_2. (**B**) – (**C**) Catalytic NO reduction by CO over different Rh catalysts under industrially relevant conditions. Reaction stream: 450 ppm NO, 2350 ppm CO, 950 ppm O_2, and 4.5 % H_2O, balanced with N_2. GHSV: 150 L g^{-1} h^{-1}. (**D**) Rh K-edge XANES spectra for Rh foil, Rh/Al_2O_3, Rh/CA10, and Rh/CA10_H. (**E**) Fourier transforms of k^3-weighted Rh K-edge EXAFS for Rh foil, Rh/Al_2O_3, Rh/CA10, and Rh/CA10_H. (**F**) CO-DRIFTS conducted at 60 ºC over different Rh catalysts. Spectra are collected after CO adsorption and helium purging.

Benefiting from the superior stability of Ce_1 (Fig. 1A and fig. S8), CeO_x/Al_2O_3 (i.e., Ce_1 or CeO_2) supported metal catalysts with well-defined hierarchical structures can be constructed. A small amount of Rh (0.1 wt %) was loaded on CAx_H via 500 °C air-calcination with controlled CeO_2 or Ce_1 coverage, where Rh was therefore associated with bare Al_2O_3, crystalline CeO_2, or dispersed Ce_1 (Fig. 2A). The catalysts were tested for NO reduction by CO under industrially relevant conditions, in the presence of O_2 and H_2O and at a high space velocity (150 L g^{-1} h^{-1}), representative for testing automotive catalysts (*25*). A second light-off activity was used as the stable performance since the air-calcined catalysts were tested under stoichiometric conditions (air/fuel ratio $\lambda = 1$) (fig. S9) (*26*). NO is mainly reduced by CO to N_2, with N_2O and NH_3 as by-products, while CO is oxidized to CO_2 by NO, O_2, and H_2O (fig. S10). Notably (Figs. 2B-2C), Rh/CA10_H exhibited the best performance at low temperatures in converting both NO and CO. The T_{50} temperatures (required for 50 % NO/CO conversions) for Rh/CA10_H are 50 °C lower than those for Rh/Al_2O_3.

To confirm the role of Rh in these catalysts, blank supports were also tested under the same condition, and were found to be totally inactive below 350 °C and 250 °C for converting NO and CO, respectively (fig. S11). Therefore, instead of bare Al_2O_3, crystalline CeO_2, or dispersed Ce_1, supported Rh species are the intrinsic active sites. The influence of the support on the nature of loaded Rh was also studied, e.g., isolated Rh_1 versus Rh or Rh_2O_3 NPs (*27*). Synchrotron-based X-ray absorption spectroscopy (XAS) was used to study the chemical state and nuclearity of supported Rh. As shown in Fig. 2D, Rh exhibits almost identical X-ray absorption near edge structures (XANES) after being loaded on Al_2O_3, CA, and CA_H, distinct from that of Rh foil, suggesting the formation of Rh cations in all catalysts. Extended X-ray absorption fine structure (EXAFS) analysis showed the dominance of Rh-O bond and absence of Rh-Rh bond in the catalysts (Fig. 2E) (*28*), indicating the single-atom nature of Rh_1 in all studied catalysts.

Diffuse reflectance infrared Fourier transform spectroscopy (DRIFTS) was conducted under flowing CO. All catalysts showed the exclusive presence of two peaks at ~ 2088 and 2015 cm^{-1} (Fig. 2F), widely ascribed to the symmetric and asymmetric CO stretches from gem-dicarbonyl complexes, i.e., $Rh_1(CO)_2$ (*27*). Combined XAS and DRIFTS results confirmed that all catalysts contain mostly Rh_1 single atoms, although the coordination structures could be slightly different due to the varied Rh_1-support interactions, as indicated by slight difference in CO-IR frequency (Fig. 2F). These Rh_1 species are stable under reducing NO-CO reaction conditions, as confirmed by DRIFTS of spent catalysts even after an *in-situ* CO reduction at 500 °C (fig. S12). Given the negligible catalytic performance of supports as well as their limited impact on Rh speciation, the greatly enhanced NO-CO reaction activity upon Ce_1 dispersion must come from changes in the local environment of active center. Therefore, isolated Rh_1 surrounded by dispersed Ce_1 is much superior to Rh_1 associated with crystalline CeO_2 or bare Al_2O_3 in catalyzing NO reduction.

To develop accurate structure-activity relationships for the rational design of Ce_1-promoted catalysts, both the local structure of Ce_1 as well as its catalytic effect need to be clarified. Strong interaction between Ce_1 and Al_2O_3 has been indicated by the outstanding thermal stability of dispersed Ce_1 (Fig. 1A), which is partially resistant to sintering even after 800 °C air calcination (fig. S13). In contrast, CeO_2 NPs are easily formed in the absence of such strong Ce_1-Al_2O_3 interaction (fig. S13). Solid-state magic angle spinning (MAS) ^{27}Al nuclear magnetic resonance (NMR) was used to investigate the structural modifications of γ-Al_2O_3. ^{27}Al MAS NMR spectra of Al_2O_3 and CA10_H in the air-exposed state showed two peaks at 11 and 70 ppm, ascribed to Al^{3+} in octahedral (Al_O) and tetrahedral (Al_T) coordination, respectively (Fig. 3A). Compared to bare γ-Al_2O_3, CA10_H showed an Al_O peak with decreased intensity and broadened shoulders,

indicating the coexistence of different Al_O sites, i.e., perturbed chemical environments of Al_O by Ce_1 (*29*). Such difference was invisible for CeO_2 NPs on Al_2O_3 (fig. S14). After dehydration, a pentahedral Al_P peak was observed in both supports at 35 ppm (*30*), while a small difference in Al_O is still discernible (fig. S15). The Al_P peak is much less pronounced in CA10_H, suggesting the consumption of Al_P as Ce_1 spreads over the Al_2O_3 surface (Fig. 3A). Therefore, both Al_P and Al_O sites contribute to stabilizing Ce_1.

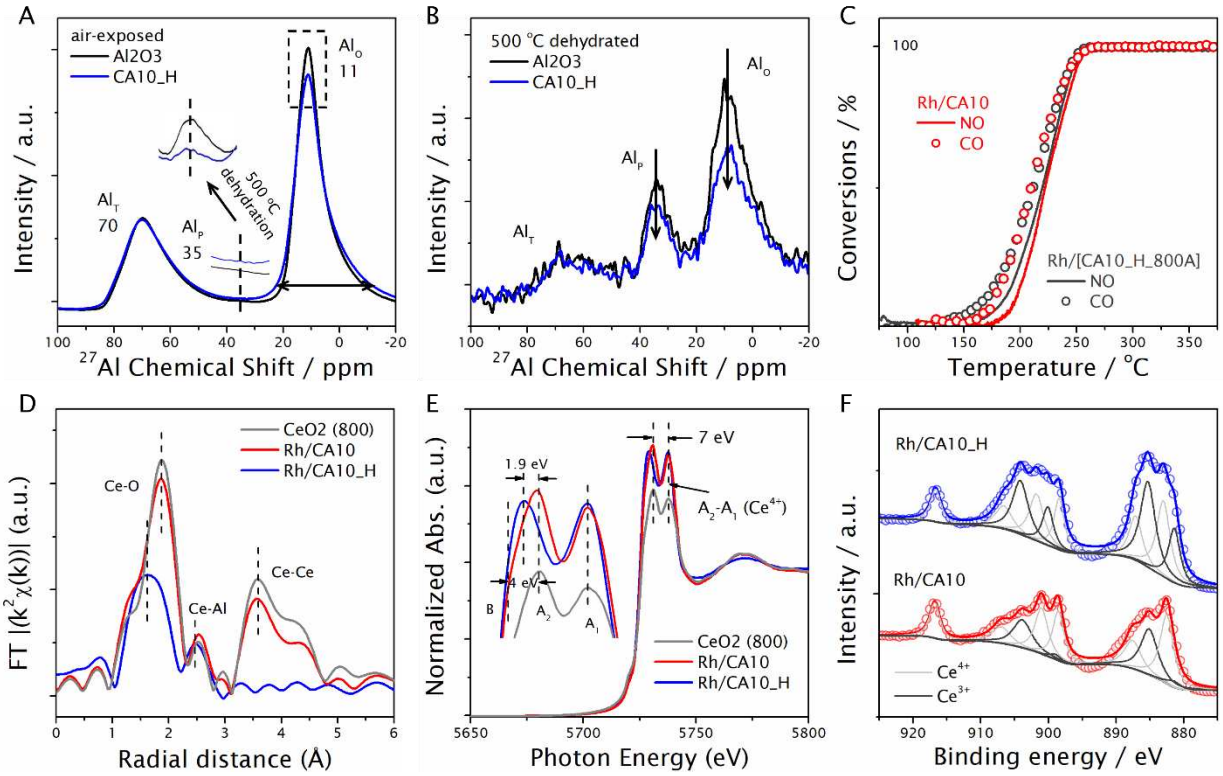

Fig. 3. Characterization and catalytic performance of Rh catalysts and supports. (**A**) Solid state ^{27}Al MAS NMR spectra of bare γ-Al_2O_3 and CA10_H in the air-exposed state. Insets show the evolution of Al_P peaks after dehydration at 500 °C. (**B**) ^1H–^{27}Al CP MAS NMR spectra of γ-Al_2O_3 and CA10_H after dehydration. Spectra were normalized by the same amount of γ-Al_2O_3. (**C**) NO-CO reaction over the Rh/CA10 and Rh/CA10_H_800A catalysts. (**D**) Normalized Ce L_{III}-edge EXAFS of 800 °C air-calcined CeO_2, Rh/CA10 and Rh/CA10_H. (**E**) Fourier transforms of Ce L_{III}-edge XANES spectra of 800 °C air-calcined CeO_2, Rh/CA10 and Rh/CA10_H. (**F**) Ce3d XPS spectra of Rh/CA10 and Rh/CA10_H.

^1H–^{27}Al cross-polarization (CP) MAS NMR that is highly surface sensitive was further used to probe Al close to surface hydroxyls (*31*). Both Al_P and Al_O peaks turned weaker with Ce_1 dispersion on Al_2O_3 surface (Fig. 3B), indicating that Ce_1 replaced hydroxyl near both Al sites, agreeing well with the statement above. Penta-Al^{3+} site has been proposed as the preferential nucleation site for different metals such like Ba, Pt, and Pd (*30, 32, 33*). Ce_1 anchored by under-coordinated Al_P should exhibit superior thermal stability to Ce_1 associated with Al_O, consistent with the observation that < 1 wt % Ce_1 existed in CA10 (fig. S3). More Ce_1-Al_P pairs are formed during Ce_1 dispersion, which can survive after prolonged air-calcination (CA10_H_800A) (fig. S13). Rh/CA10_H_800A exhibited similar activity compared to Rh/CA10 (Fig. 3C), suggesting that Ce_1 strongly anchored by Al_P made limited contribution to the promoted NO reduction over Rh/CAx_H (Figs. 2B and 2C).

XAS was conducted to examine the chemical environments of dispersed Ce_1. As shown in the Ce L_{III}-edge EXAFS spectra, Rh/CA10 shows both intense Ce-O and Ce-Ce features, similar to air-calcined CeO_2 (Fig. 3D). Interference from Rh is negligible due to the low loading. In contrast, Rh/CA10_H shows a shorter Ce-O bond (2.2 vs. 2.3 Å) with a coordination number of 7.3 ± 1.5 and a second Ce-Al shell (Ce-O-Al) at 3 Å (fig. S16 and table S1), confirming the exclusive presence of dispersed Ce_1 after Rh loading at 500 °C. The short Ce-O/Al distances explain the outstanding thermal stability of Ce_1. As shown in the Ce L_{III}-edge XANES spectra (Fig. 3E), both CeO_2 and Rh/CA10 show two prominent absorption peaks (A_1 and A_2) separated by 7 eV, transitions diagnostic of Ce^{4+}. In comparison, Rh/CA10_H shows a shifted A_2 feature towards lower energies by 1.9 eV. The characteristic B transition of Ce^{3+} is absent, which is ~ 4 eV lower than A_2 (*34*). This suggests that Rh/CA10_H contains a mixture of Ce^{3+} and Ce^{4+}. The reduced valency of Ce_1 was further confirmed by X-ray photoelectron spectroscopy (XPS) that the Ce^{3+} content increased from ~ 31 % in Rh/CA10 to ~ 45 % in Rh/CA10_H (Fig. 3F). Besides Ce_1 dispersion, high-temperature reduction also induced surface electron enrichment as indicated by the slightly lower Al2p and O1s energies in CA10_H (figs. S17 and S18).

With clarified Ce_1-Al_2O_3 structures, the catalytic effects of dispersed Ce_1 can be discussed in detail. The promoting role of nanosized CeO_2 in catalysis stems from the facile oxygen transfer within the fluorite lattice, generally evaluated by oxygen storage capacity (OSC) (*2*). OSC was measured for unsupported CeO_2, Al_2O_3-supported CeO_2 (CA10), and Ce_1 on Al_2O_3 (CA10_H). CeO_2 calcined at lower temperatures (500 vs. 800 °C) or supported on Al_2O_3 (CeO_2 vs. CA10) shows higher OSC (Fig. 4A), due to smaller particle size and rich defects. Surprisingly, although without structural integrity, Ce_1 on Al_2O_3 shows ~ 3-4 times higher OSC than crystalline CeO_2, approaching 2.1 mmol/g CeO_2 at 350 °C, 73 % of the theoretical maximum (Fig. 4A). The high OSC of CA10_H was maintained after 500 °C calcination (1.9 mmol/g) but drastically decreased (0.8 mmol/g) after 800 °C calcination (fig. S19). This fully agrees with the structural evolution of Ce_1 upon controlled aging (Fig. 1A), confirming that the greatly enhanced OSC of CA10_H is associated with Ce_1 being dispersed on the Al_2O_3 surface.

Such enhanced OSC of Ce_1/Al_2O_3 should benefit redox reactions on supported metals, e.g., Rh_1-catalyzed NO reduction which is mediated by oxygen transfer between NO and CO. Kinetic studies were conducted on Rh/CAx_H ($0 < x < 16$) to further understand the promoting role of dispersed Ce_1. As confirmed, up to 10 wt % CeO_2 can be fully dispersed into Ce_1 after the high-temperature reduction (CA10_H), beyond which crystalline CeO_2 coexisted (fig. S4). Notably, with increased amount of Ce_1 on Al_2O_3, the reaction rate of isolated Rh_1 at 250 °C increased linearly from 1.1 min^{-1} for Rh/Al_2O_3 to 10.1 min^{-1} for Rh/CA10_H (Fig. 4B). This also indicates the random nucleation of Rh on Ce_1/Al_2O_3 considering that 2 wt % Ce_1 would be sufficient to anchor 0.1 wt % Rh_1. Further increased CeO_2, which beyond 10 wt % persists even after high-temperature reduction, resulted in decreased reaction rates (Fig. 4B). This agrees well with the light-off results (Fig. 2B), validating the superiority of Ce_1 in promoting the Rh-catalyzed NO reduction.

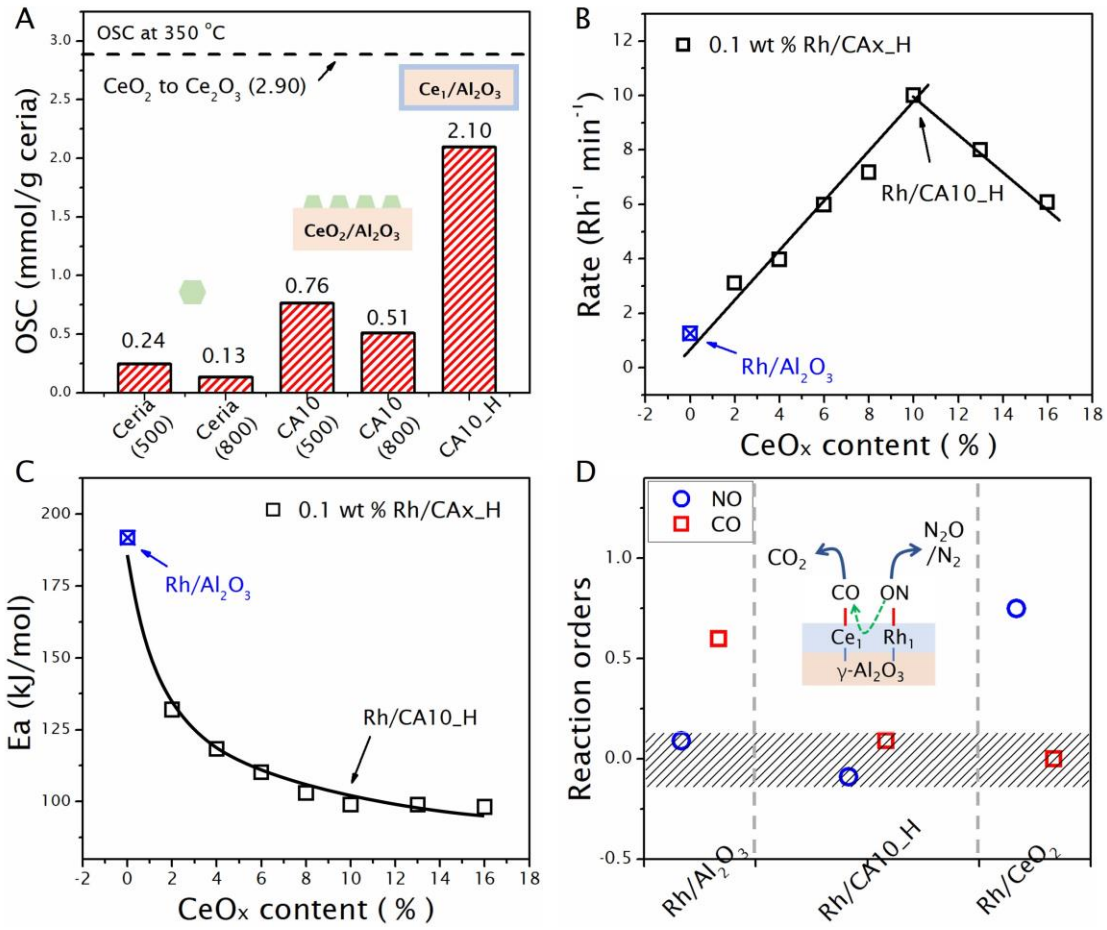

Fig. 4. Characterization and kinetic studies of Rh catalysts and supports. (**A**) oxygen storage capacity (OSC) measurements of CeO_2, CA10, and CA10_H. (**B**) Reaction rates of NO reduction over Rh/CAx_H (0 < x <16) measured at 250 °C under differential NO conversions, normalized by Rh_1. Conditions: 1000 ppm NO, 2000 ppm CO, N_2 balance. (**C**) Apparent activation energies (E_a) of Rh on Al_2O_3, CA10, and CAx_H (0 < x <16). Conditions: 1000 ppm NO, 2000 ppm CO, N_2 balance, 250-275 °C. (**D**) NO reduction rate dependence on partial pressures of NO (500-1400 ppm) and CO (1000-4000 ppm) at 260 °C. Inset is the proposed reaction scheme between activated NO and CO on neighbored Rh_1/Ce_1 single-atom pairs.

Dispersed Ce_1 on Al_2O_3 greatly lowered the apparent activation energy (E_a) for NO reduction from 192 kJ/mol (Rh/Al_2O_3) to 96 kJ/mol (Rh/CA10_H), which remained almost constant with further increased CeO_2 content (Fig. 4C and fig. S20). This indicates that Ce_1 has substantially modified the mechanism of Rh_1-catalyzed NO-CO reaction. Zhang et al. proposed for NO-CO reaction over single-atom Rh_1 on SiO_2, the step with the highest energy barrier is the coupling between the activated NO* and CO* that are co-adsorbed on isolated Rh_1 (*35*). The calculated barrier (2.16 eV, 208 kJ/mol) is very close to Ea that we observed for Rh/Al_2O_3 in this work. Reaction rate dependence on the partial pressures of reactants (pCO/pNO) were measured over different Rh catalysts to shed light on the mechanism change upon Ce_1 dispersion (fig. S21). In contrast to Rh/Al_2O_3 which exhibited a positive order for CO (0.6) and a ~ 0 order for NO, and Rh/CeO_2 which exhibited a positive order for NO (0.75) and a ~ 0 order for CO, Rh/CA10_H exhibited ~ 0 orders for both NO and CO (Fig. 4D). Apparently, Ce_1 has weakened the kinetic relevance of reactant activation on the adjacent Rh_1 center in one Ce_1-Rh_1 pair.

Based on these OSC and kinetic measurements, a reaction model for the NO-CO reaction on isolated Rh_1 supported on Ce_1-modified γ-Al_2O_3 ($Rh_1/Ce_1/Al_2O_3$) is proposed, as indicated by the inset of Fig. 4D. In contrast to Rh/Al_2O_3 where NO and CO are co-adsorbed on one Rh_1 site, in the proposed model, NO and CO are adsorbed on isolated Rh_1 and neighboring Ce_1 cations, respectively. The superior oxygen shuttling mediated by dispersed Ce_1 greatly promotes the reaction between the adsorbed Rh_1-NO* and Ce_1-CO* with a substantially decreased energy barrier, namely, the greatly promoted redox cycles. With promoted in CO activation and NO*-CO* reaction by Ce_1, Rh_1 on the Ce_1-modified γ-Al_2O_3 presents excellent NO reduction at low temperatures.

Recent interest in single-atom catalysis has been mostly focused on the effect of dispersing active metals. Here, we demonstrate that controlled dispersion of catalytic promoters which have been widely used in industrial catalysts can also substantially influence the activities of the integrated system. The understanding of reductive atom trapping of Ce_1 as well as its structure-property relationships obtained in this work could be implemented in the rational design of Ce_1-promoted catalysts for many other applications. Benefiting from the greatly enhanced OSC, we found that dispersed Ce_1 on Al_2O_3 also promotes the catalytic performance of supported Pt NPs (figs. S22 and S23) in the oxidation of CO and hydrocarbons (fig. S24). Additionally, dispersing Ce_1 on Al_2O_3 results in modified surface properties, including the formation of weaker acid sites (figs. S25 and S26) and the overall enhanced surface basicity (fig. S27). The observations could be further utilized to explore the field of acid-base catalysis.

References

1. C. Sun, H. Li, L. Chen, Nanostructured ceria-based materials: synthesis, properties, and applications. *Energy Environmental Science* **5**, 8475-8505 (2012).
2. A. Trovarelli, Catalytic properties of ceria and CeO2-containing materials. *Catalysis Reviews* **38**, 439-520 (1996).
3. D. Jiang *et al.*, Elucidation of the Active Sites in Single-Atom Pd1/CeO2 Catalysts for Low-Temperature CO Oxidation. *ACS Catalysis* **10**, 11356-11364 (2020).
4. Y. Li *et al.*, Dynamic structure of active sites in ceria-supported Pt catalysts for the water gas shift reaction. *Nature Communications* **12**, 914 (2021).
5. H. Sun *et al.*, Boosting Activity on Co4N Porous Nanosheet by Coupling CeO2 for Efficient Electrochemical Overall Water Splitting at High Current Densities. *Adv. Funct. Mater.* **30**, 1910596 (2020).
6. D. Jiang, W. Wang, L. Zhang, Y. Zheng, Z. Wang, Insights into the Surface-Defect Dependence of Photoreactivity over CeO2 Nanocrystals with Well-Defined Crystal Facets. *ACS Catalysis*, 4851-4858 (2015).
7. R. Si, M. Flytzani-Stephanopoulos, Shape and Crystal-Plane Effects of Nanoscale Ceria on the Activity of Au-CeO2 Catalysts for the Water–Gas Shift Reaction. *Angew. Chem. Int. Ed.* **47**, 2884-2887 (2008).
8. Z. Hu, H. Metiu, Effect of Dopants on the Energy of Oxygen-Vacancy Formation at the Surface of Ceria: Local or Global? *The Journal of Physical Chemistry C* **115**, 17898-17909 (2011).
9. R. Alcala *et al.*, Atomically Dispersed Dopants for Stabilizing Ceria Surface Area. *Applied Catalysis B: Environmental* **284**, 119722 (2021).

10. Q. An *et al.*, Cerium-Catalyzed C–H Functionalizations of Alkanes Utilizing Alcohols as Hydrogen Atom Transfer Agents. *Journal of the American Chemical Society* **142**, 6216-6226 (2020).
11. H. Tsurugi, K. Mashima, Renaissance of Homogeneous Cerium Catalysts with Unique Ce(IV/III) Couple: Redox-Mediated Organic Transformations Involving Homolysis of Ce(IV)–Ligand Covalent Bonds. *Journal of the American Chemical Society* **143**, 7879-7890 (2021).
12. Y. Xia, M. Sayed, L. Zhang, B. Cheng, J. Yu, Single-atom heterogeneous photocatalysts. *Chem Catalysis*, (2021).
13. H. Xu, D. Cheng, D. Cao, X. C. Zeng, A universal principle for a rational design of single-atom electrocatalysts. *Nature Catalysis* **1**, 339-348 (2018).
14. F. Zaera, Designing Sites in Heterogeneous Catalysis: Are We Reaching Selectivities Competitive With Those of Homogeneous Catalysts? *Chemical Reviews*, (2022).
15. S. Hinokuma *et al.*, Subnano-particle Ce catalyst prepared by pulsed arc-plasma process. *Catalysis Communications* **54**, 81-85 (2014).
16. K. A. Ledwa, L. Kepinski, M. Pawlyta, Atomically dispersed cerium species in NMxCe1-xO2/Al2O3 (NM = Rh, Ru) catalysts. *Materials Research Bulletin* **122**, 110673 (2020).
17. S. Luo *et al.*, Hierarchical Heterogeneity at the CeOx–TiO2 Interface: Electronic and Geometric Structural Influence on the Photocatalytic Activity of Oxide on Oxide Nanostructures. *The Journal of Physical Chemistry C* **119**, 2669-2679 (2015).
18. H. N. Pham *et al.*, Designing Ceria/Alumina for Efficient Trapping of Platinum Single Atoms. *ACS Sustainable Chemistry & Engineering*, (2022).
19. M. Yoo *et al.*, A tailored oxide interface creates dense Pt single-atom catalysts with high catalytic activity. *Energy & Environmental Science* **13**, 1231-1239 (2020).
20. K. Konstantin, Dramatic improvement of NO reduction activity via reversible re-dispersion of CeO2 nanoparticles into Ce+3 atoms on alumina under high temperature reactive treatment *ChemRxiv*, (2021).
21. H. Jeong *et al.*, Highly durable metal ensemble catalysts with full dispersion for automotive applications beyond single-atom catalysts. *Nature Catalysis*, (2020).
22. J. Shyu, W. Weber, H. Gandhi, Surface characterization of alumina-supported ceria. *The Journal of Physical Chemistry* **92**, 4964-4970 (1988).
23. M. Zhu *et al.*, Combining in-situ TEM observations and theoretical calculation for revealing the thermal stability of CeO2 nanoflowers. *Nano Research*, (2021).
24. M. A. Małecka, L. Kępiński, New, intermediate polymorph of CeAlO3 with hexagonal structure – formation and thermal stability. *CrystEngComm* **17**, 2273-2278 (2015).
25. K. G. Rappé *et al.*, Aftertreatment Protocols for Catalyst Characterization and Performance Evaluation: Low-Temperature Oxidation, Storage, Three-Way, and NH3-SCR Catalyst Test Protocols. *Emission Control Science and Technology* **5**, 183-214 (2019).
26. B. Zhao *et al.*, Insight into the effects of different ageing protocols on Rh/Al2O3 catalyst. *Applied Surface Science* **308**, 230-236 (2014).
27. C. Asokan, Y. Yang, A. Dang, A. B. Getsoian, P. Christopher, Low-Temperature Ammonia Production during NO Reduction by CO Is Due to Atomically Dispersed Rhodium Active Sites. *ACS Catalysis* **10**, 5217-5222 (2020).
28. M. Machida *et al.*, Catalyst Deactivation via Rhodium–Support Interactions under High-Temperature Oxidizing Conditions: A Comparative Study on Hexaaluminates versus Al2O3. *ACS Catalysis* **11**, 9462-9470 (2021).

29. C. Wan *et al.*, Investigating the Surface Structure of γ-Al2O3 Supported WOX Catalysts by High Field 27Al MAS NMR and Electronic Structure Calculations. *The Journal of Physical Chemistry C* **120**, 23093-23103 (2016).
30. J. H. Kwak *et al.*, Coordinatively Unsaturated Al3+ Centers as Binding Sites for Active Catalyst Phases of Platinum on g-Al2O3. *Science* **325**, 1670-1673 (2009).
31. A. T. F. Batista *et al.*, Beyond γ-Al2O3 crystallite surfaces: The hidden features of edges revealed by solid-state 1H NMR and DFT calculations. *Journal of Catalysis* **378**, 140-143 (2019).
32. H. Duan *et al.*, Pentacoordinated Al3+-Stabilized Active Pd Structures on Al2O3-Coated Palladium Catalysts for Methane Combustion. *Angewandte Chemie International Edition* **58**, 12043-12048 (2019).
33. J. H. Kwak, J. Z. Hu, D. H. Kim, J. Szanyi, C. H. F. Peden, Penta-coordinated Al3+ ions as preferential nucleation sites for BaO on γ-Al2O3: An ultra-high-magnetic field 27Al MAS NMR study. *Journal of Catalysis* **251**, 189-194 (2007).
34. R. G. Agarwal, H.-J. Kim, J. M. Mayer, Nanoparticle O–H Bond Dissociation Free Energies from Equilibrium Measurements of Cerium Oxide Colloids. *Journal of the American Chemical Society* **143**, 2896-2907 (2021).
35. S. Zhang *et al.*, Catalysis on Singly Dispersed Rh Atoms Anchored on an Inert Support. *ACS Catalysis* **8**, 110-121 (2018).

Acknowledgments:

This work was supported by the U.S. Department of Energy (DOE), Energy Efficiency and Renewable Energy (EERE), Vehicle Technologies Office (DE-FOA-0002197). Work at the Molecular Foundry was supported by the Office of Science, Office of Basic Energy Sciences, of the U.S. Department of Energy under Contract No. DE-AC02-05CH11231. This study used resources of the Advanced Photon Source, an Office of Science User Facility operated for the U.S. DOE Office of Science by Argonne National Laboratory and was supported by U.S. DOE under Contract DE-AC02-06CH11357, and the Canadian Light Source and its funding partners. Use of the Stanford Synchrotron Radiation Light source, SLAC National Accelerator Laboratory, is supported by the U.S. Department of Energy, Office of Science, Office of Basic Energy Sciences under Contract DE-AC02-76SF00515. The authors thank A. Benavidez for her help with part of XPS measurements.

Competing interests: Authors declare no competing interests.

Data and materials availability: All data are available in the main text or the supplementary materials.

Supplementary Materials

Materials and Methods

Figs. S1 to S27

Tables S1

References (36-40)

Supplementary Materials

Materials and Experimental Methods

Chemicals and Catalyst Synthesis

Gamma phase aluminum oxide (γ-Al_2O_3) (CATALOX SBa-150) from Sasol was pre-calcined at 850 °C in air and used as the catalyst support. Cerium (III) nitrate hexahydrate ($Ce(NO_3)_3 \cdot 6H_2O$, 99.99 %) obtained from Sigma Aldrich was used as the precursor of CeO_2. Rhodium (III) nitrate hydrate ($N_3O_9Rh \cdot xH_2O$, ~ 36 % rhodium Rh basis) obtained from Sigma Aldrich was used as the precursor of supported Rh. Deionized water (DI-H_2O) was used during the synthesis.

CeO_2/Al_2O_3. CeO_2 supported on Al_2O_3 was prepared *via* incipient wetness impregnation followed by 800 °C air calcination for 6 hours. Specifically, different amounts (2-19 wt % CeO_2) of $Ce(NO_3)_3 \cdot 6H_2O$ was dissolved into an appropriate amount of DI-H_2O (0.45 ml/g alumina) and then impregnated on Al_2O_3. The powders were dried overnight at 80 °C followed by calcination in static air at 800 °C with a ramp of 5 °C min^{-1}. The resulting catalyst was denoted as CAx (CA02-CA19), indicating the content of CeO_2 from 2 to 19 wt % in the obtained powders.

Ce/Al_2O_3. Atomically dispersed Ce atoms on Al_2O_3 surface were obtained by a reducing post-treatment of above prepared CA (CeO_2/Al_2O_3) mixed oxide. Specifically, powders of CA were reduced in 10 % H_2/He at 800 °C for 10 hours with a ramp of 5 °C/min. After cooling down to room temperature, the reduced powders were directly exposed to air and then calcined in static air at 200 °C for 1 hour before being used to support Rh. These reduced supports were denoted as CAx_H (e.g., CA02_H to CA19_H). CA10_H was also further calcined in static air at 500 °C and 800 °C, termed as CA10_H_500A and CA10_H_800A, respectively.

Single-atom Rh catalysts. 0.1 wt % Rh was loaded on the surface of various supports *via* incipient wetness impregnation followed by air calcination at 500 °C for 6 hours. For example, Rh/CA10_H is 0.1 wt % Rh loaded on the surface of a pre-reduced CA10.

Pt colloidal NPs: 0.1 g $Pt(acac)_2$ was mixed with 30 mL oleyl amine and degassed at 100 °C for 0.5 h. Under the N_2 atmosphere, 0.4 g Borane tert-butylamine complex dissolved in 6-8 mL oleyl amine was quickly injected into the solution. The solution was then ramped to 120 °C with a rate of 2 °C/min and kept at 120 °C for 1 h. The obtained black solution was then washed with a mixture of isopropanol/hexanes (4/1) once and twice with a mixture of ethanol/hexanes (4/1). Supernatant was disposed and the NPs were dispersed in hexanes for further use.

Supported Pt NPs catalysts. 0.8 wt % Pt colloidal NPs were deposited on bare Al_2O_3, CA10, and CA10_H via wet impregnation method followed by air calcination at 500 °C for 2h. Specifically, 220 mg of each support was mixed with 15 ml hexane (Sigma Aldrich, HPLC Grade) in a centrifuge tube. 0.44 ml of Pt (4 mg/ml, 1.76 mg of Pt) was injected into the centrifuge tube under vigorous stirring at room temperature. The mixture was stirred overnight. Afterwards, the solid was recovered by centrifugation. Colorless supernatants were observed for all catalysts, indicating the complete adsorption of Pt NPs onto the supports. Final powders were dried overnight at 80 °C followed by air calcination.

Materials Characterization

X-ray diffraction (XRD) measurements were conducted on a Rigaku SmartLab with the 2 Theta from 15 to 85 °, using a scanning rate of 1 °/min at a step of 0.02°. The employed radiation was Cu K-α with a wavelength of 0.154 nm. The Brunauer, Emmett and Teller (BET) surface areas were determined by a Micromeritics TriStar II 3020 using N_2 adsorption at -196 °C. The visible

(532 nm) Raman spectra were collected at room temperature (RT) using a Horiba LabRAM HR Raman/FTIR microscope equipped with a Synapse Charge Coupled Device (CCD) camera.

Electron Spectroscopy

Sample powders were dispersed in ethanol and then mounted on the holey carbon grids for examination in a JEOL NeoARM 200CF transmission electron microscope which is equipped with spherical aberration correction to allow atomic resolution imaging, and an Oxford Aztec Energy Dispersive System (EDS) for elemental analysis. The microscope is equipped with two large area EDS detectors for higher throughput in acquisition of x-ray fluorescence signals. Images were recorded in annular dark field (ADF) mode and in annular bright field (ABF) mode.

X-ray Absorption Spectroscopy

XAS for the Ce L_3-edge (5723.0 eV) spectra were recorded at the Stanford Synchrotron Radiation Lightsource (SSRL, California, USA) at wiggler beamline 4–3, using a Si(111) $\phi = 0°$ double-crystal monochromator. The storage ring was operated at 3 GeV with a ring current of 494–500 mA in top-up mode. The incident x-rays were monochromatized using a Si (111) double crystal monochromator which was detuned to 80% of flux maximum at the Ce L_3-edge to minimize the higher harmonics. To minimize the X-ray absorption along the X-ray path, the beam path was mostly filled with He and the sample was placed in a He filled box. The intensity of the incident and transmitted x-rays was monitored using He filled ion chambers. Samples were measured in both transmission mode using ion chamber and fluorescence mode using a 4-element solid-state silicon drift detector. The CeO_2 reference was scanned simultaneously with each sample for energy calibration. Monochromator energy calibration was done using Ce foil spectrum by setting the first inflection point at 5723.0 eV. The data for a CeO_2 standard were recorded in transmission mode after dilution with boron nitride (~5% w/w). The XAS data reduction was carried out with the SamView program included in SixPack software package (http://www.sams-xrays.com/sixpack). Athena software, Demeter version 0.9.26 was used for data processing and analysis (*36*). For each catalyst, three scans were collected and merged after alignment. $\chi(k)$ was obtained by subtracting the smooth atomic background from the normalized absorption coefficient using the AUTOBK code. The theoretical EXAFS signals for Ce−O, Ce−Ce, and Ce−Al paths for different samples were generated using the FEFF6 code (*37*). The theoretical EXAFS signals were fitted to the data in *R*-space using Artemis by varying the coordination numbers of the single scattering paths, the effective scattering lengths, the bond length disorder, and the correction to the threshold energy, ΔE_0 (common for all paths since they are all from the same FEFF calculation). S_0^2 (the passive electron reduction factor) was obtained by first analyzing the spectrum for the bulk CeO_2 (Sigma Aldrich, fit with first shell Ce−O as 8), and the best fit value (0.60) was fixed in the fit. The *k*-range used for fitting was 2.2− 9.3 $Å^{-1}$, while the *R*-range was 1−3.15 Å for the model that includes Ce−O and Ce−Al scattering shell and 1.4−4.7 Å for the model that includes Ce−O and Ce−Ce scattering paths. The best parameters fit using *k*-weights of 2 in Artemis are reported. Additionally, small differences in the *k*-range did not have a significant effect on the best fit values of the model fit but did affect their uncertainties. The XANES and EXAFS measurements at Rh K-edge were conducted at the beamline 20-ID in Advanced Photon Source, Argonne National Laboratory in the fluorescence mode, a Rh foil was measured simultaneously in transmission mode. The data was analyzed using Athena software.

Activity Measurements

Catalytic measurements of above catalysts were conducted using a fixed bed flow reactor at atmospheric pressure. 120 mg of catalyst powders (150 µm) diluted by 1 g SiC was packed inside a quartz tube (I.D. 1/2 inch) with coarse frit in the middle. For NO reduction by CO, reaction gas consisted of 450 ppm NO, 2350 ppm CO, 950 ppm O_2, and 4.5 % H_2O, balanced with N_2 with a total flow of 300 ml min^{-1}. The weight hourly space velocity (GHSV) is 150,000 ml g^{-1} h^{-1}. H_2O vapor was introduced into the stream by an in-line temperature-controlled bubbler. For lean oxidation of CO and hydrocarbons (HCs), reaction gas consisted of 0.3 % CO, 0.1 % propane (C_3H_8), 0.1 % propylene (C_3H_6), and 3 % O_2 balanced with N_2 with a total flow of 300 ml min^{-1}. The GHSV is 150,000 ml g^{-1} h^{-1}. The effluent gas was analyzed by online continuous FTIR MKS MultiGas™ Analyzer equipped with a LN-cooled MCT detector. The light-off curves (LOCs) were collected from room temperature to 500 °C with a ramp of 5 °C/min and cooled down in reaction gas before the next run. For each catalyst, two or three sequential LOCs were collected, and the 2nd LOC was confirmed to be the stable and representative performance.

Kinetic Measurements

Kinetic studies were conducted under slightly rich (reducing) NO-CO conditions. Both apparent activation energy (E_a) and reaction orders on NO/CO over different Rh/Al_2O_3, Rh/CA, and Rh/CA_H catalysts were tested under differential NO/CO conversions (< 10 %) by adjusting the GHSV. For E_a estimation, 1000 ppm NO + 2000 ppm CO was used as reaction stream and reaction rates were measured between 250 to 275 °C. Reaction orders were measured at 260 °C. For NO dependence, CO was fixed at 2000 ppm, meanwhile, NO was changed from 500 ppm to 1500 ppm. For CO dependence, NO was fixed at 1000 ppm, meanwhile, CO was changed from 1000 to 4000 ppm. Since both CO-DRIFTS and EXAFS studies indicated that supported Rh are mostly isolated Rh atoms. Turnover frequency (TOF) was calculated using the number of NO/CO molecules converted per second divided by the total number of Rh atoms.

Infrared Spectroscopy

IR in the diffuse reflectance mode was conducted on a Tensor 27 spectrometer (Bruker) equipped with a DRIFTS cell (Harrick Scientific Inc.). The catalyst powders were loaded in the DRIFTS cell and pre-treated at 400 °C in 10 % O_2 for 30 min before cooling down to specific temperatures for background collection.

CO-DRIFTS. In situ infrared spectroscopy was conducted in a diffuse reflectance mode using CO as a probe molecule. A Tensor 27 spectrometer (Bruker) equipped with a DRIFTS cell (Harrick Scientific Inc.) was employed. For pre-treatment, the Rh catalyst powders were loaded in the DRIFTS cell and heated at 350 °C in flowing 10 % O_2 for 30 min and helium for 15 min, consecutively. Afterwards, the sample cell was cooled down in helium to 60 °C and the background spectrum was collected. Then the gas flow was switched to 1 % CO balanced with helium for CO adsorption for 30 min. Afterwards, the cell was purged by helium to remove gaseous and weakly adsorbed CO. DRIFTS spectra were collected every 1 min.

Pyridine-DRIFTS (IR-Py). Types of acid sites (i.e., Lewis vs Brönsted) were assessed using Diffuse Reflectance Infrared Fourier Transform Spectroscopy (DRIFTS) of chemisorbed pyridine. Approximately 20mg of the catalytic sample was loaded into the *in-situ* cell (Harrick Scientific products inc.) and were analyzed with a Bruker Tensor 27 FTIR spectrometer. Prior to pyridine dosing, catalysts underwent *in situ* pretreatment in 20 sccm 10 % O_2/He at 450 °C for 1 hr. The temperature was decreased to 100 °C at 10 °C/min, pausing at temperature points of 450, 300, 260, 200, and 100 °C to acquire background scans of the sample. Pyridine was introduced to the

catalytic surface at 100 ºC via a bubble generator with 10 ml/min of flowing He. The dosing of pyridine continued until the IR signal was invariant with time. The cell was then purged with 50 ml/min He for 1 h before beginning the temperature ramp to remove any physiosorbed pyridine. The temperature was then increased at 10 ºC/min while continuously flowing 50 ml/min He during the experiment. Each temperature point was held for 5 minutes before acquiring the spectra.

Chemisorption

NH_3 and CO_2 temperature programmed desorption measurements (NH_3 /CO_2-TPD) were conducted on Autochem 2920 (Micromeritics). Catalyst powders (100 mg) were placed in a U-shaped quartz tube reactor. Desorption of NH_3 and CO_2 was monitored using a QMS equipped with a Secondary Electron Multiplier detector. Ar (5 % Ar/He was used as carrier gas) was used as an internal standard to normalize the other signals.

NH_3-TPD. Sample powders were first treated in flowing 5 % Ar/He at 500 ºC for 30 min and then cooled down to 100 ºC. Then, NH_3 adsorption was conducted using 10 % NH_3 in helium at 100 ºC for 30 min. Afterwards, sample was purged in flowing 5 % Ar/He at the same temperature for 180 min to fully desorb the weakly adsorbed NH_3 on the surface. At last, the reactor was heated up to 600 ºC with a ramp of 10 ºC/min. Meanwhile, the evolved NH_3 was monitored by an on-line QMS.

CO_2-TPD. Sample powders were first treated in flowing 5 % Ar/He at 500 ºC for 30 min and then cooled down to - 50 ºC. Then, CO_2 adsorption was conducted using 10 % CO_2 in helium at - 50 ºC for 30 min. Afterwards, sample was purged in flowing 5 % Ar/He at the same temperature for 180 min to fully desorb the weakly adsorbed CO_2 on the surface. At last, the reactor was heated up to 400 ºC with a ramp of 10 ºC/min. Meanwhile, the evolved CO_2 was monitored by an on-line QMS.

Oxygen Storage Capacity

OSC measurements were conducted using Autochem 2920 (Micromeritics). Sample powders (100 mg) were placed in a U-shaped quartz reactor. Before OSC measurements, the loaded sample was pretreated at different temperatures (e.g., 350-800 ºC) in flowing 10 % O_2/He for 30 min and cooled down to 350 ºC in He. Sample was then treated in 2 % O_2/He at 350 ºC for 20 min as oxygen saturation step, followed by He purging at the same temperature for 20 min to remove adsorbed O_2. Afterwards, 2 % CO/He flowed through the sample for 20 min. An online QMS was used to monitor the evolution of CO_2, quantified as the OSC value.

Nuclear Magnetic Resonance

^{27}Al and ^{1}H MAS NMR experiments were conducted with a 14.0921 T Bruker 600WB spectrometer utilizing a commercial 2.5 mm pencil-type MAS probe. The Larmor frequency of ^{27}Al and ^{1}H are 156.4 MHz and 600 MHz respectively. Before the NMR pulse experiments, samples were calcined in air atmosphere at 500 °C at the flow rate of 50 ml/min for 1 h. Then the quartz tube was sealed and transferred to glovebox. The treated samples (about 10 mg) were then packed into 2.5 mm rotor (*38*). ^{27}Al single pulse experiments were implemented with a 45° pulse width of 0.75 us, a recycle delay time of 1s. Typically, 5000 scans were collected to allow for reasonable signal to noise ratios. ^{1}H single pulse MAS NMR experiments were utilized to detect surface -OH species on each sample. ^{1}H single pulse experiments were conducted with a pulse width of 6.5 us, a recycle delay time of 1 s. Typically, 100 scans were collected to allow for reasonable signal to noise ratios. ^{1}H-^{27}Al cross polarization NMR was employed to investigate the

distance and interaction between ^{1}H and surface ^{27}Al. A $\pi/2$ pulse width of 4 μs for ^{1}H with a 4 s recycle delay and a contact time of 1.5 ms was applied. ^{1}H and ^{27}Al chemical shifts were calibrated with adamantane and 1M $Al(NO_3)_3$ as secondary references at 1.82 ppm and 0 ppm, respectively (*39*).

X-ray Photoelectron Spectroscopy

The X-ray photoelectron spectroscopy (XPS) measurements were performed using the K-Alpha XPS System from Thermo Scientific. The photon source was a monochromatized Al K α line ($h\nu$ = 1486.6 eV). The spectra were acquired using a spot size of 400 μm and constant pass energy. A combined low energy electron/ion flood source was used for charge neutralization. All spectra were energy corrected by the Ce^{4+} $3d_{5/2}$ component at 916.7 eV (*40*).

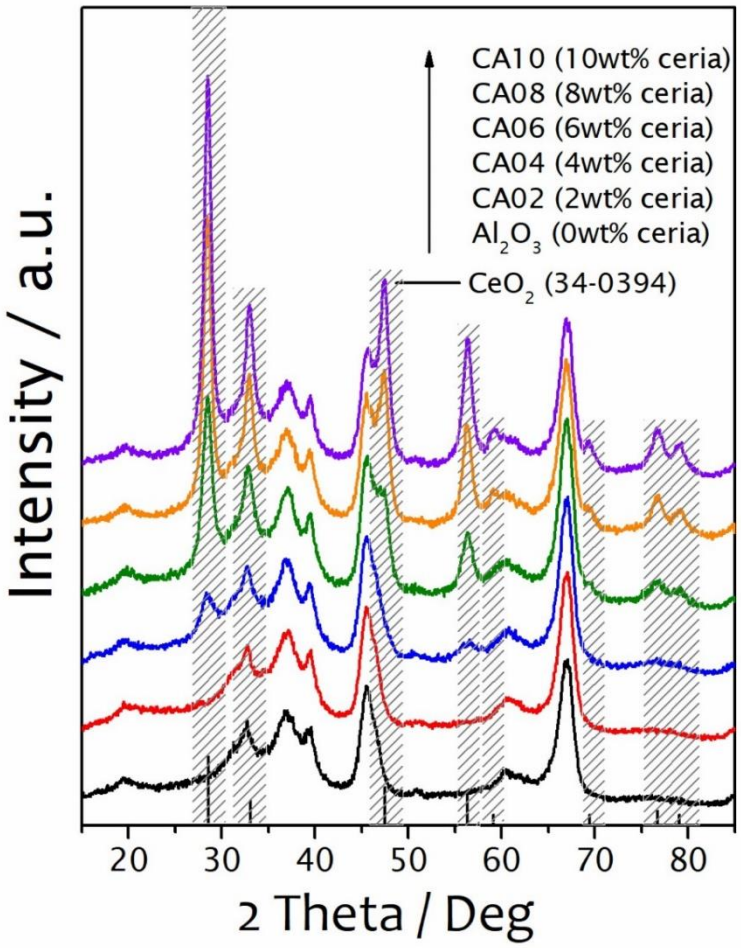

Fig. S1. Powder X-ray diffraction (XRD) patterns of commercial gamma-phase γ-Al_2O_3 and different CeO_2-Al_2O_3 mixture with an increasing loading of CeO_2 from 2-10 wt %, i.e., CA02-CA10. Standard profiles of fluorite CeO_2 (#34-0394) are showed for reference.

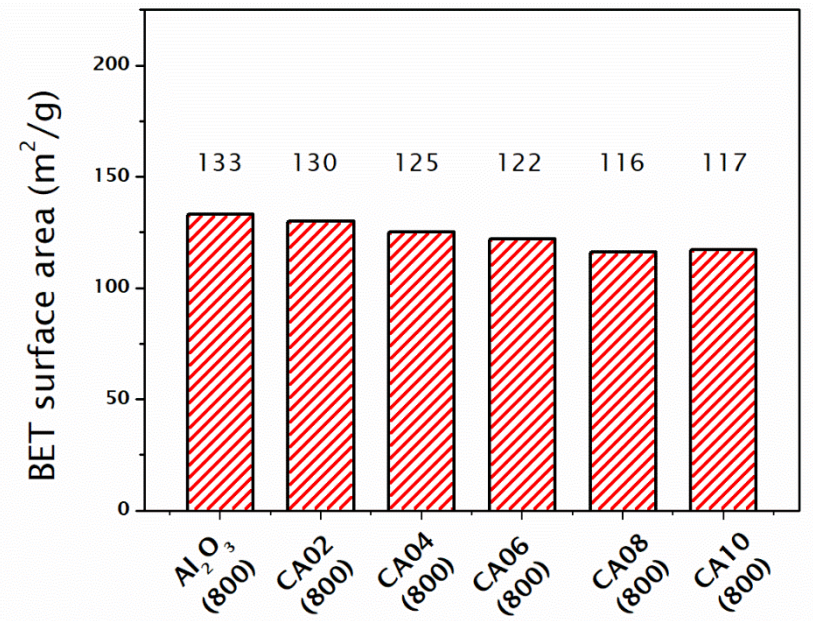

Fig. S2. BET surface areas of commercial gamma-phase γ-Al_2O_3 and various mixed oxide CeO_2-Al_2O_3 compounds with an increasing loading of CeO_2 from 2 to 10 wt %, i.e., CA02-CA10. All powders are calcined at 800 °C in air before BET measurements and serving as catalyst supports.

For CAx (x < 2 wt %), isolated Ce atoms may present on Al_2O_3 surface which do not contribute to the surface area due to the zero-dimensional nature. For CAx (2 < x < 10 wt %), CeO_2 forms crystalline NPs (10 nm grain size based on XRD, probably bigger particle size) contribute much less to the surface area than Al_2O_3. Therefore, the resulted CAx compounds showed decreased BET surface area with the addition of increased amount of CeO_2 (Ce precursor).

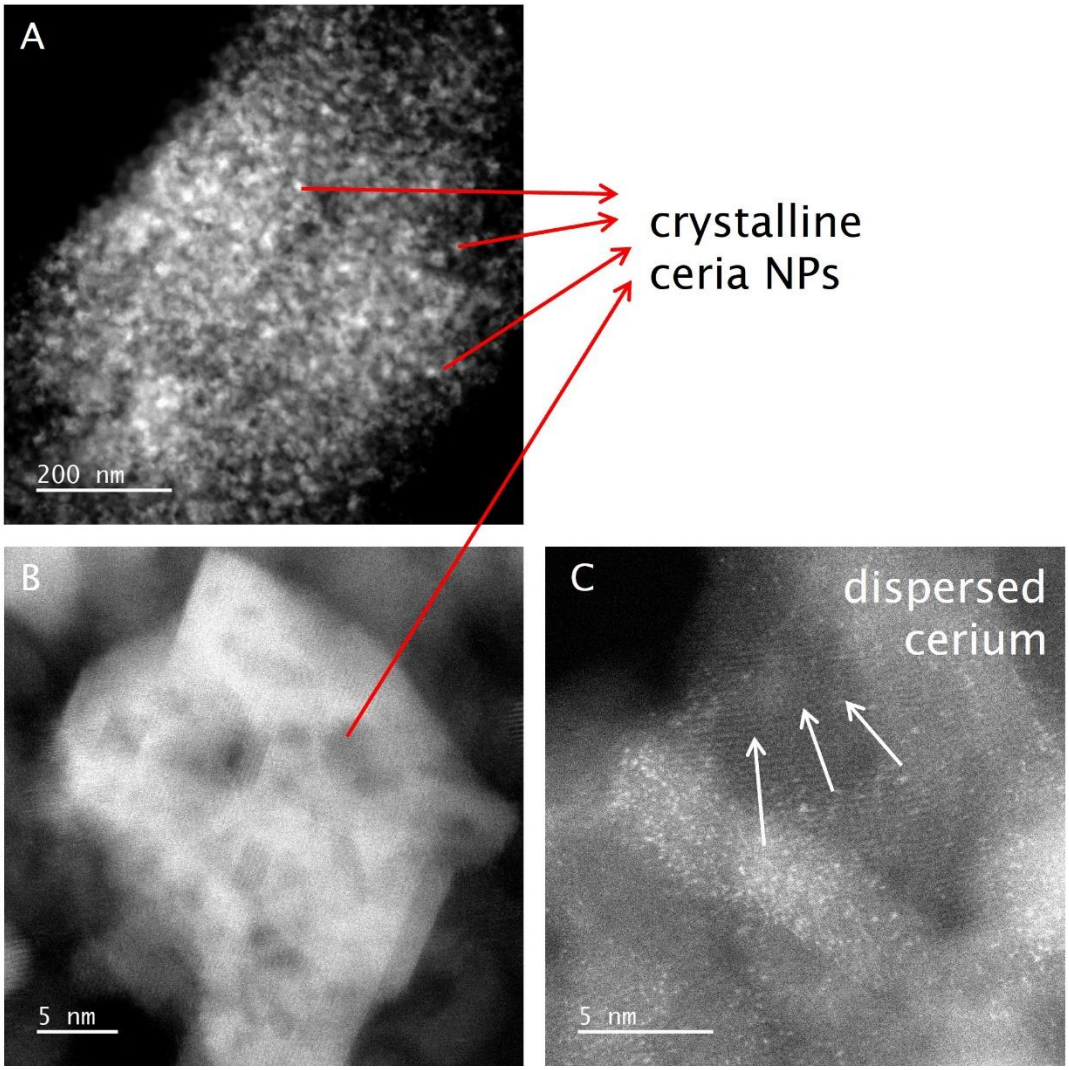

Fig. S3. (A) AC-STEM image of air-calcined CA10 at a low magnification showing the dominant presence of CeO_2 NPs on Al_2O_3 surface. (B) – (C) AC-STEM images showing the typical CeO_2 NPs (B) and the presence of a small amount (0.7 wt %) of dispersed Ce (C) in CA10 (A).

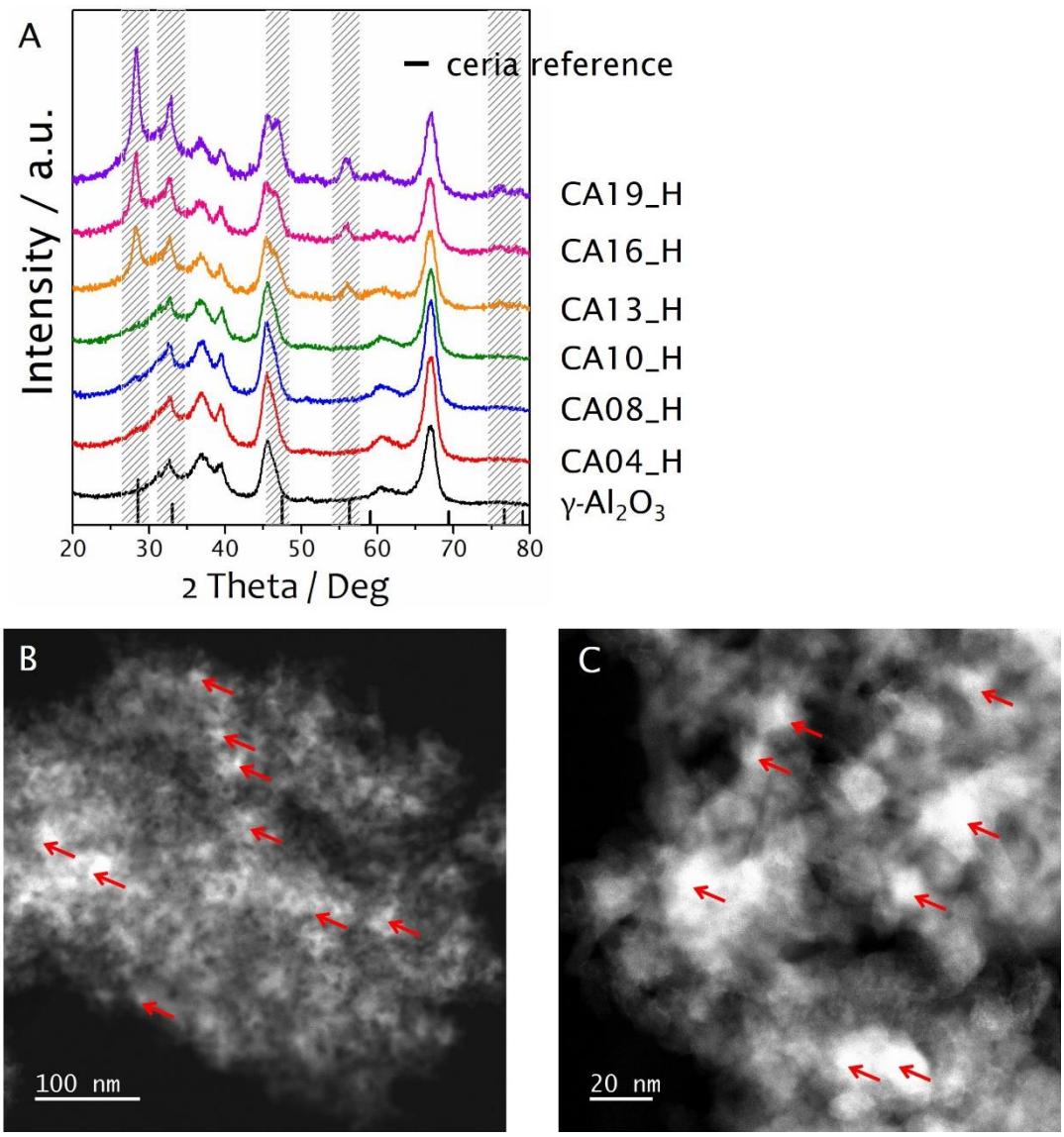

Fig. S4. (A) Powder X-ray diffraction (XRD) patterns of different CA04-CA19 samples after identical 800 °C high-temperature H_2 reduction, i.e., CAx_H. (B) – (C) AC-STEM images of CA16_H showing the existence of crystalline CeO_2 even after the H_2 treatment. Arrows indicate the presence of CeO_2 NPs.

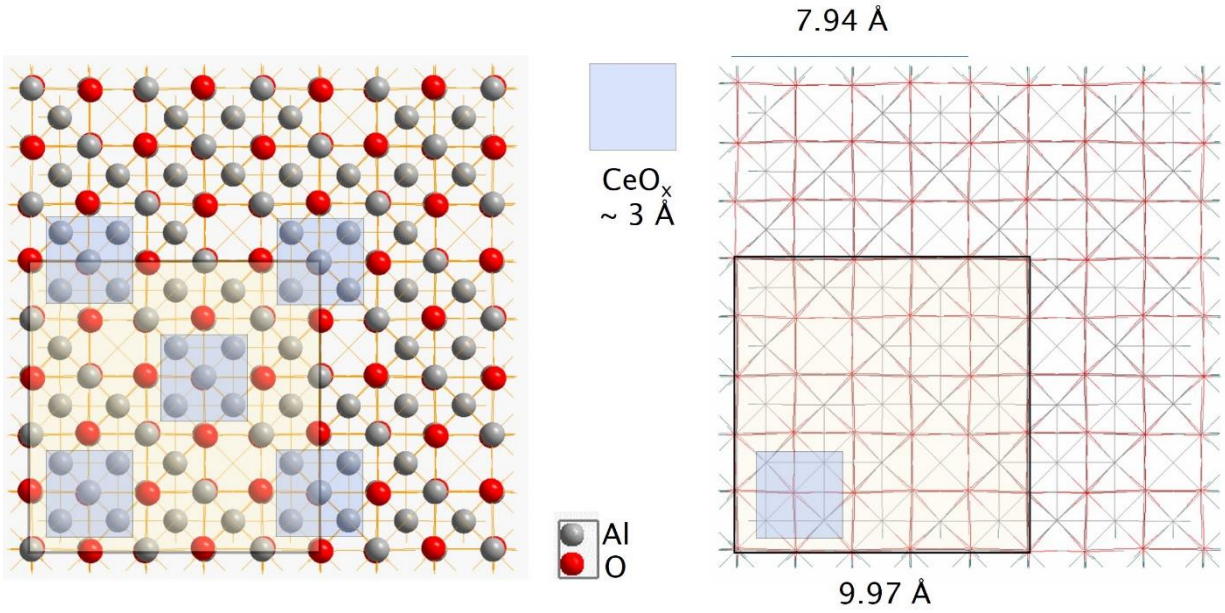

Fig. S5. A model of $CeO_x/\gamma\text{-}Al_2O_3$ (100) interface, assuming a cubic structure of $\gamma\text{-}Al_2O_3$. One 9.97 x 9,97 $Å^2$ sized square is used to indicate the Al_2O_3 surface. CeO_x is roughly represented by a 2.7 x 2.7 $Å^2$ sized square, the projection of a CeO_8 cube of ceria.

Calculation of surface CeO_x density in CA10_H

Considering CA10 containing 90 wt % Al_2O_3 (S_{BET} = 133 m^2/g) and 10 wt % CeO_2, CeO_2 will be reduced to atomically dispersed CeO_x (e.g., Ce or $CeO_{1.5}$) on the surface of Al_2O_3. For 1 g of CA10, the exposed surface area after 800 °C calcination in air is ~ 105 (90 % of S_{CA10}) to 120 m^2 (90 % of S_{Al2O3}). The surface density of CeO_x in CA10_H is estimated to be ~ 3.0-3.5 nm^{-2}, higher than half-monolayer coverage. A maximum (monolayer coverage) is estimated to be ~ 6 Ce/nm^2 in one previous report (*16*).

Atomic wight of CeO_2: M [g mol^{-1}]
Molar quantity of CeO_x species: n [mol] = 0.1g / M
Number of CeO_x species: $N = N_A * n$
Surface density of CeO_x in CA10_H: $\rho = N/S_{Al2O3}$

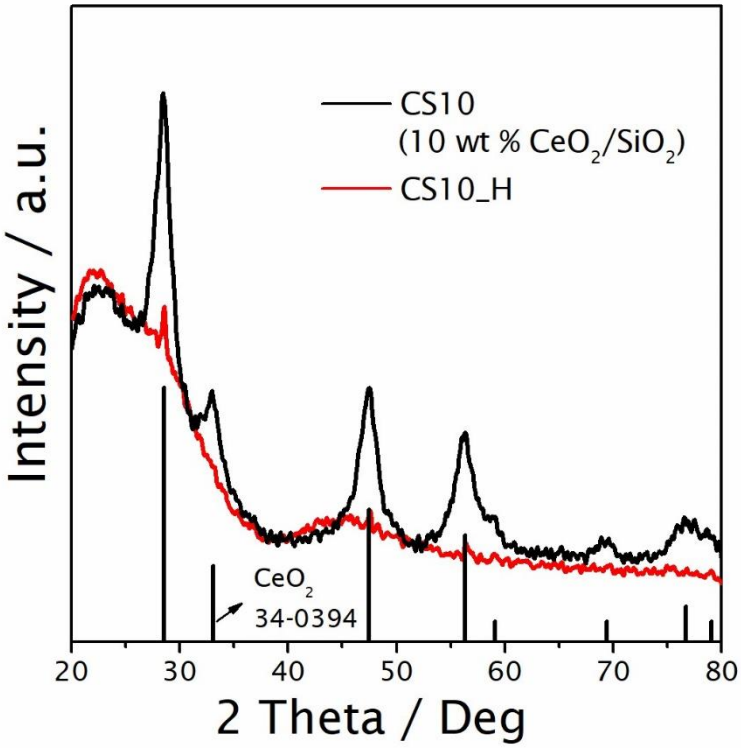

Fig. S6. Powder X-ray diffraction (XRD) patterns of the 10 wt % CeO_2 deposited on SiO_2 (CS10) and the reduced CS10_H after a 10 % H_2 reduction AT 800 oC for 10 h. Standard profiles of fluorite CeO_2 (#34-0394) are shown for reference.

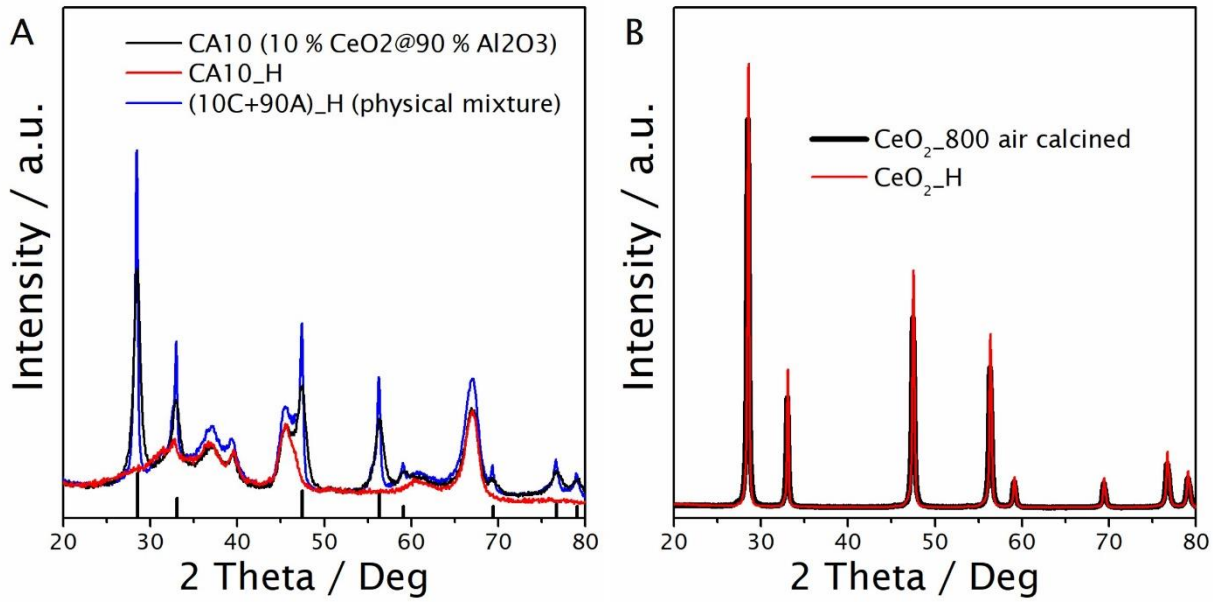

Fig. S7. (A) Powder X-ray diffraction (XRD) patterns of CA10, CA10_H, and a physical mixture of 10 wt % CeO_2 and 90 wt % Al_2O_3 after identical 10 % H_2 reduction at 800 °C for 10 h. Standard profiles of fluorite CeO_2 (#34-0394) are shown for reference. (B) XRD patterns of an air calcined CeO_2 and the H_2-reduced CeO_2_H.

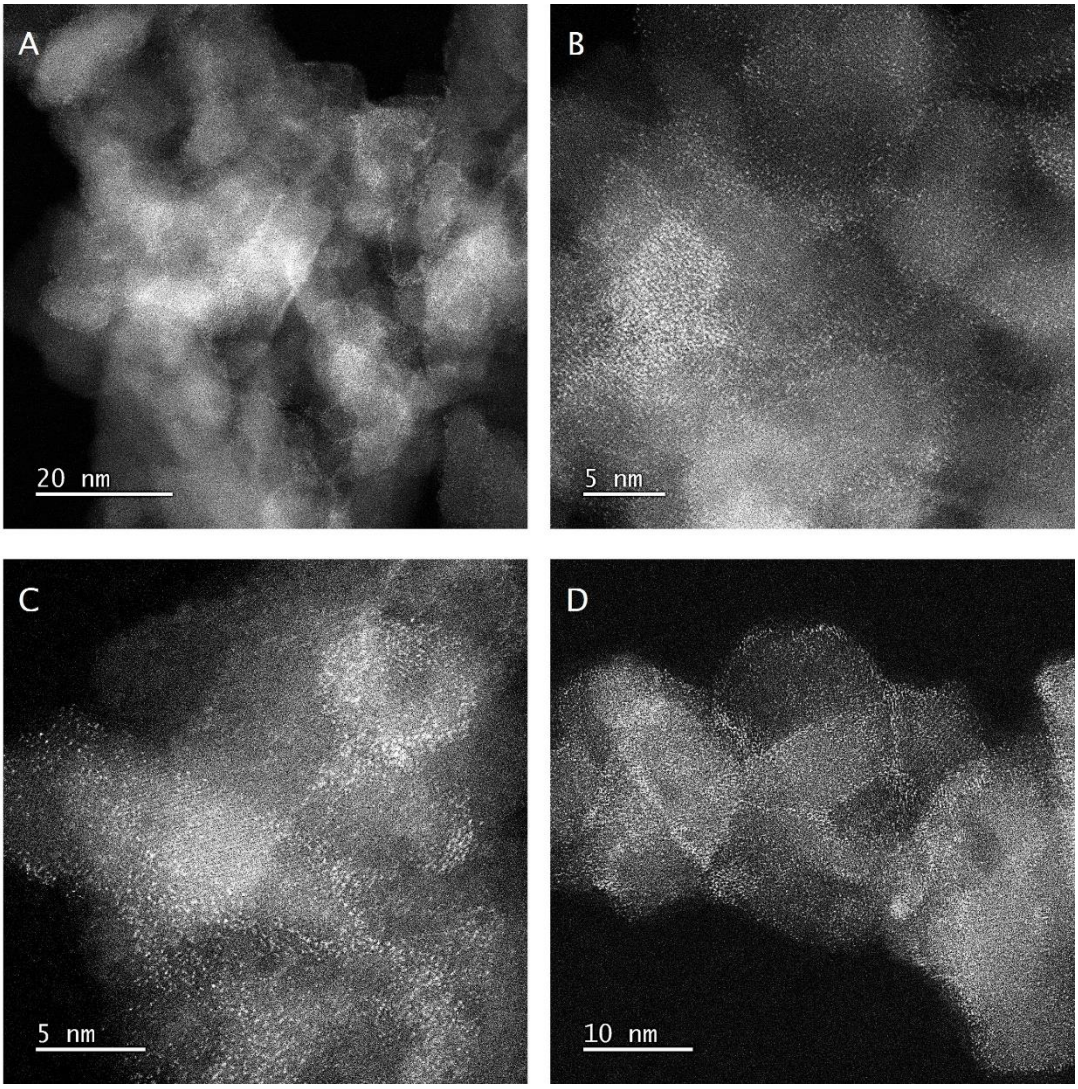

Fig. S8. STEM images of CA06_H (A-B) and CA10_H (C-D) after post-calcination in air at 500 ºC (CAx_H_500A) for 6 hours, showing that almost all the dispersed Ce species are maintained. The bright dots come from isolated, atomically dispersed, Ce atoms on the alumina surface.

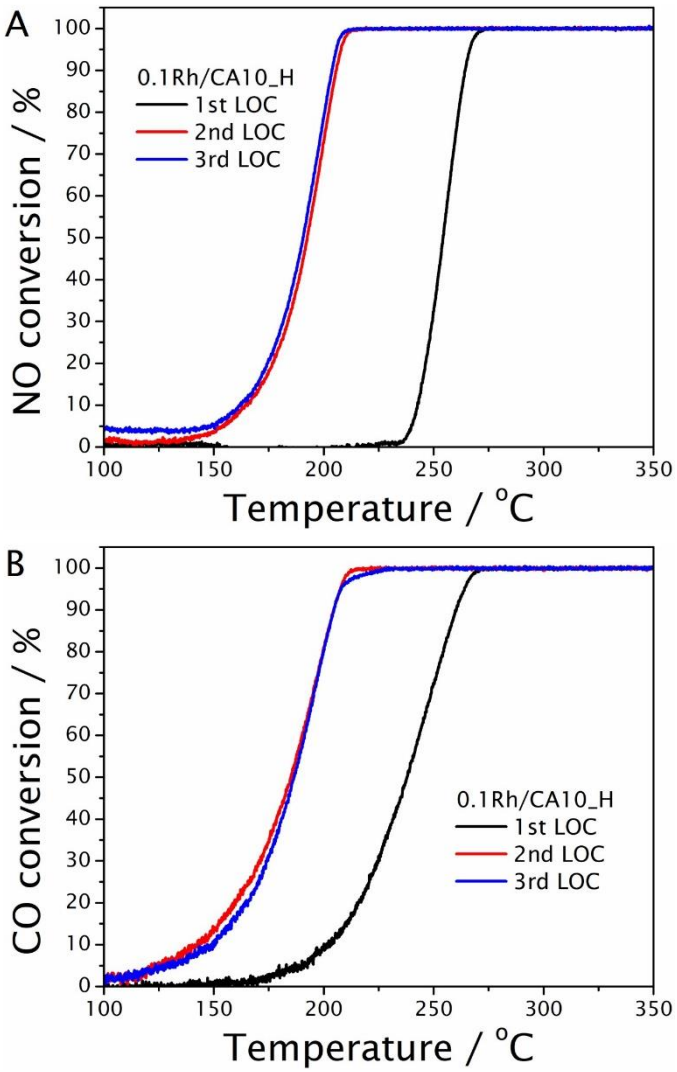

Fig. S9. Three successive light-off curves (LOCs) of NO-CO reaction over as-synthesized 0.1 % Rh/CA10_H catalyst, clearly showing that the 2nd LOC represents the stable state of this catalyst. Reaction stream: 450 ppm NO, 2350 ppm CO, 950 ppm O_2, and 4.5 % H_2O, balanced with N_2. GHSV: 150,000 ml g^{-1} h^{-1}.

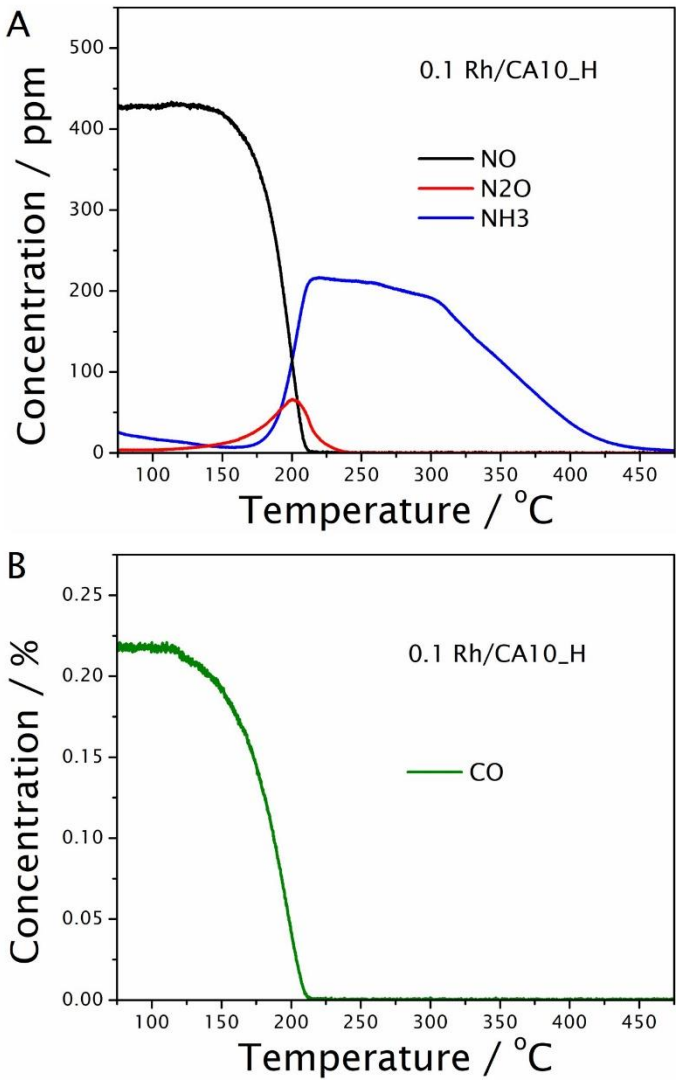

Fig. S10. Gas concentration profiles versus temperature during the light off over 0.1 % Rh/CA10_H catalyst. The second LOC was shown. Conditions: 450 ppm NO, 2350 ppm CO, 950 ppm O_2, and 4.5 % H_2O, balanced with N_2. GHSV: 150,000 ml g^{-1} h^{-1}.

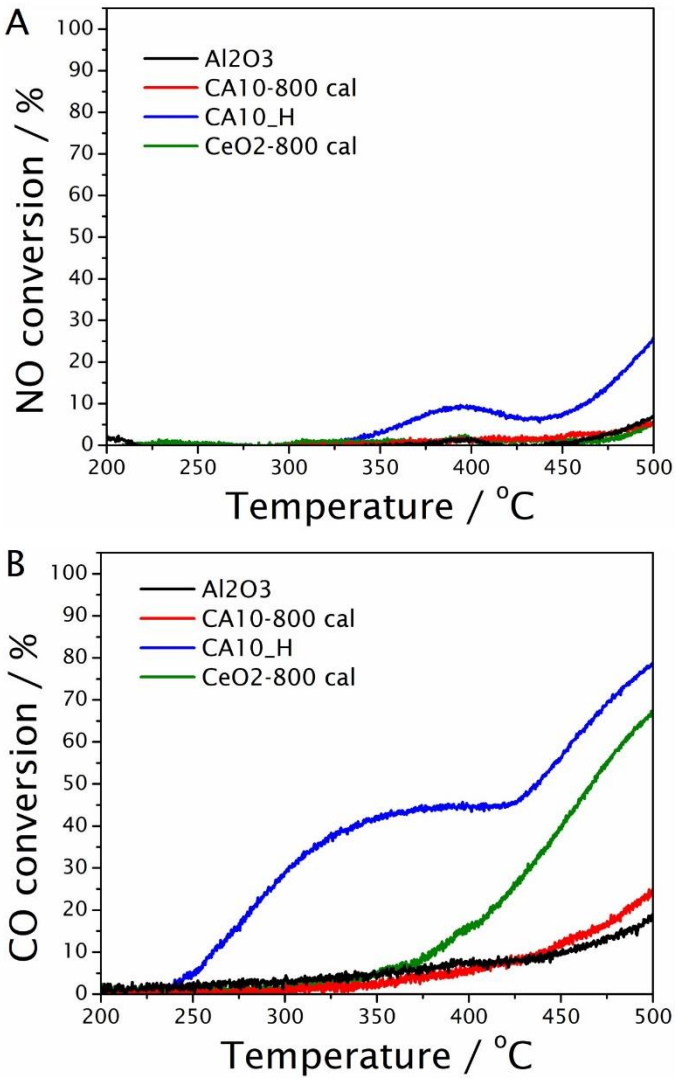

Fig. S11. NO and CO conversions during NO-CO reaction over different Al_2O_3 and CA supports. The second LOC was shown. Conditions: 450 ppm NO, 2350 ppm CO, 950 ppm O_2, and 4.5 % H_2O, balanced with N_2. GHSV: 150,000 ml g^{-1} h^{-1}.

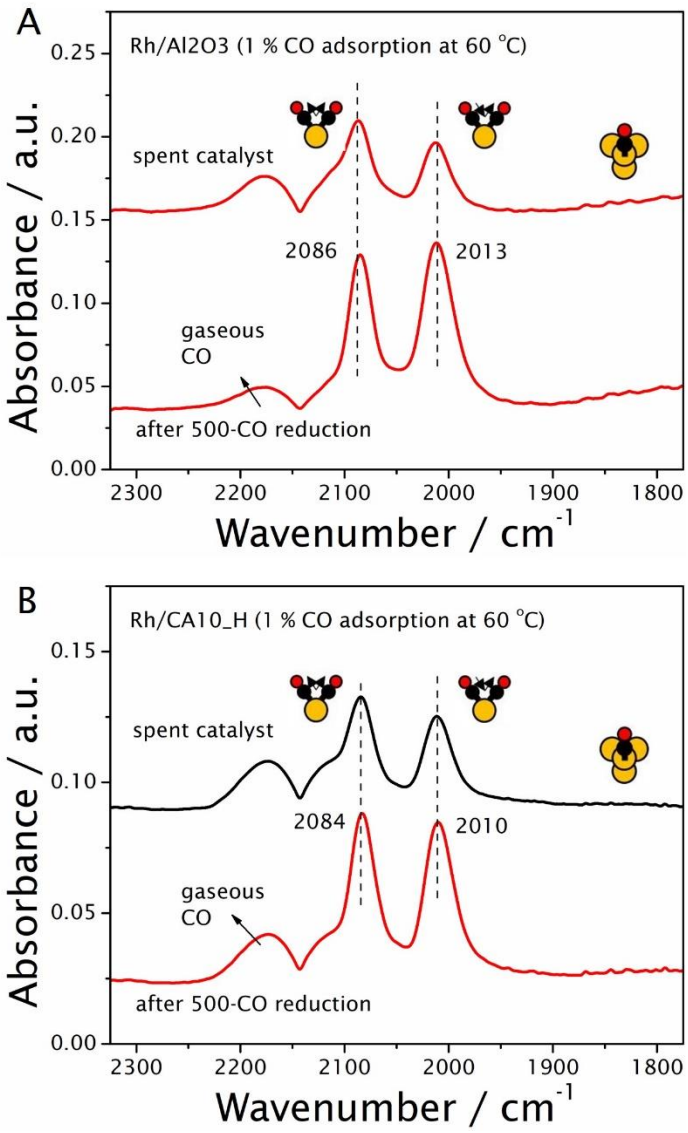

Fig. S12. CO-DRIFTS conducted at 60 °C in 1 % CO over the spent 0.1 wt % Rh/Al_2O_3 and 0.1 wt % Rh/CA10_H catalysts after typical pre-treatment (350 °C in O_2 followed by He -purging) and *in-situ* CO reduction at 500 °C for 30 min.

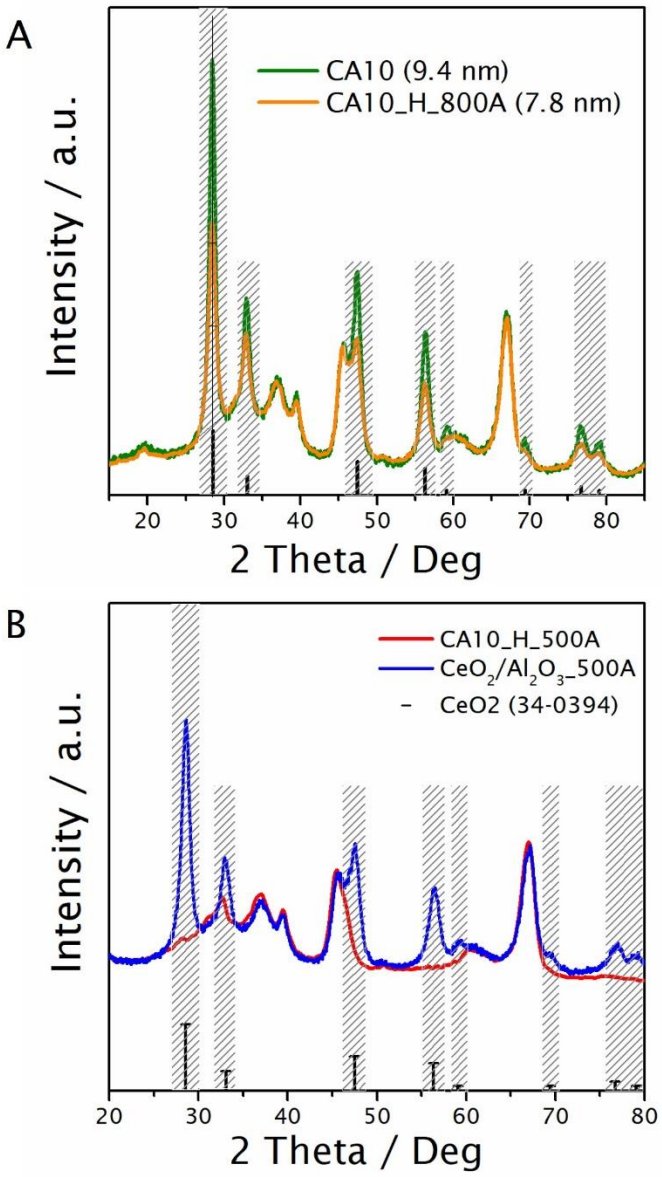

Fig. S13. (A) X-ray diffraction (XRD) patterns of CA10 and CA10_H_800A, showing that some of the dispersed Ce were even resistant to sintering after 800 oC air calcination (800A). (B) XRD patterns of CA10_H_500A and CeO_2/Al_2O_3_500A, showing that CeO_2 NPs easily formed when loading $Ce(NO_3)_3$ on Al_2O_3 followed by 500 ^oC air calcination.

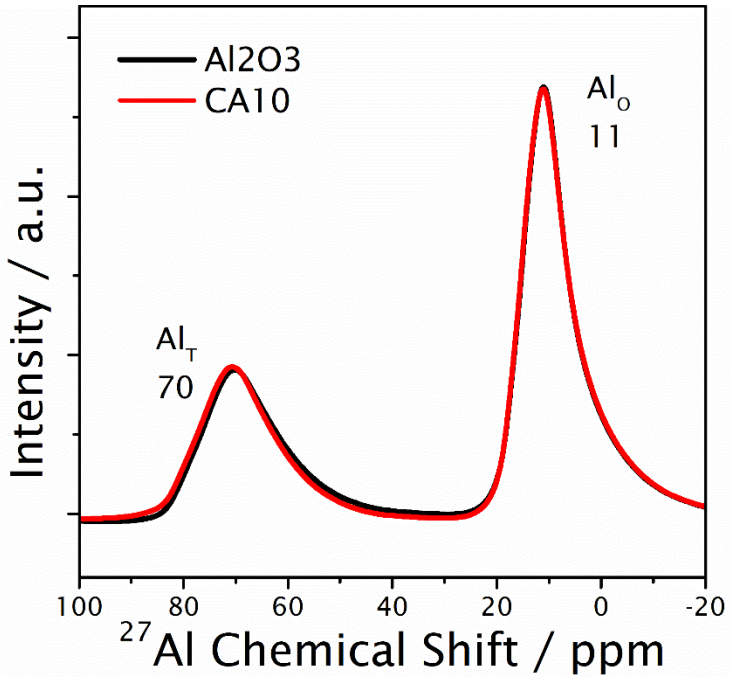

Fig. S14. Solid state ^{27}Al MAS NMR spectra of bare γ-Al_2O_3 and CA10 in the air-exposed state, showing that CeO_2 loading on Al_2O_3 didn't modify the chemical environments of the octa-Al sites.

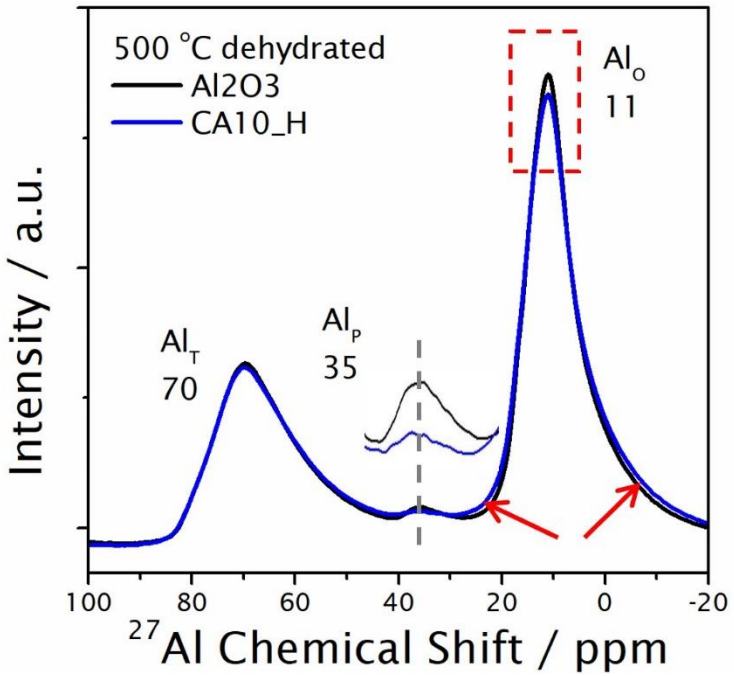

Fig. S15. Solid state ^{27}Al MAS NMR spectra of γ-Al_2O_3 and CA10_H after dehydration at 500 °C with the tetrahedral (Al_T), octahedral (Al_O) and penta-coordinated (Al_P) features indicated. The inset is the Al_P peak of the two supports enlarged for comparison.

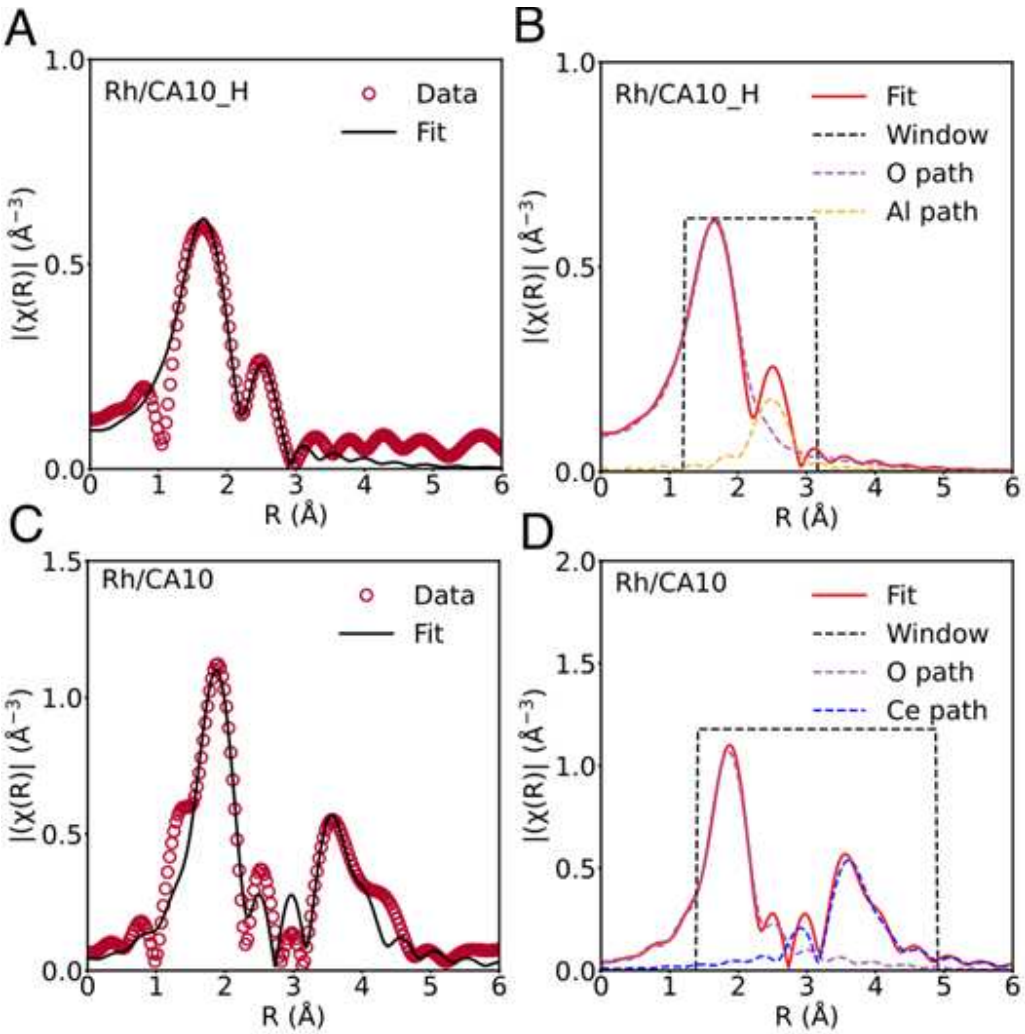

Fig. S16. EXAFS multiple shell analysis of Rh/CA10_H (A, B) and Rh/CA10 (C, D) at Ce L_{III}-edge. Total fit signal (black line) superimposed on the experimental signal (red dot) in A and C. Fit signal, fit window, Ce-O and Ce-Al path in C. Fit signal, fit window, Ce-O and Ce-Ce path in D. *k*: 2.2–9.3 $Å^{-1}$. *R*: 1–3.15 Å.

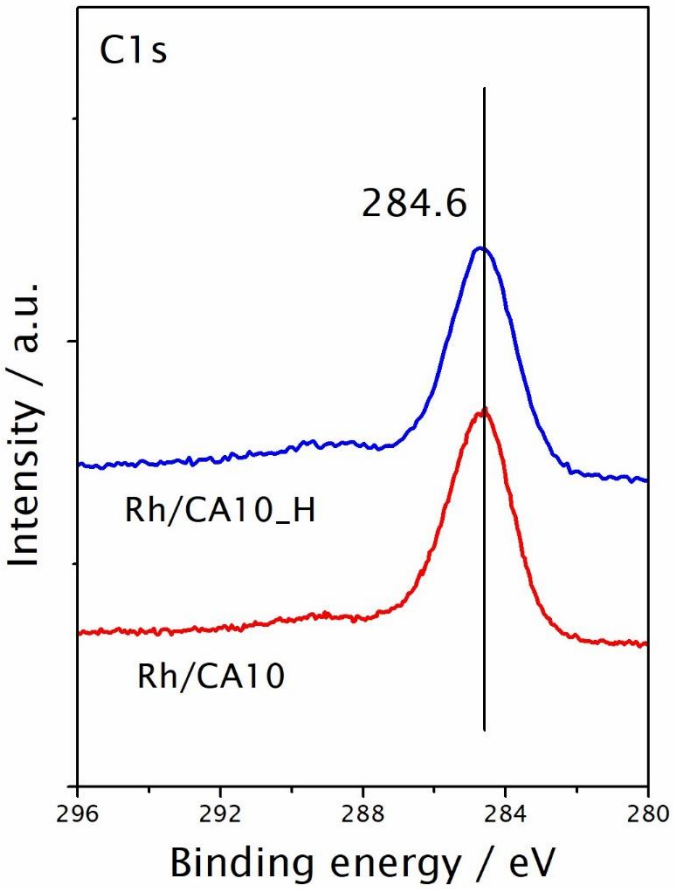

Fig. S17. C1s XPS spectra of Rh/CA10 and Rh/CA10_H. After correcting the energy of spectra by the Ce^{4+} $3d_{5/2}$ component at 916.7 eV (*40*). The C1s peak of both samples are located at 284.6 eV, which is another widely employed charge correction component. This confirms the appropriateness of energy correction. Therefore, comparison of the peak positions of other elements (e.g., Al2p and O1s) is meaningful.

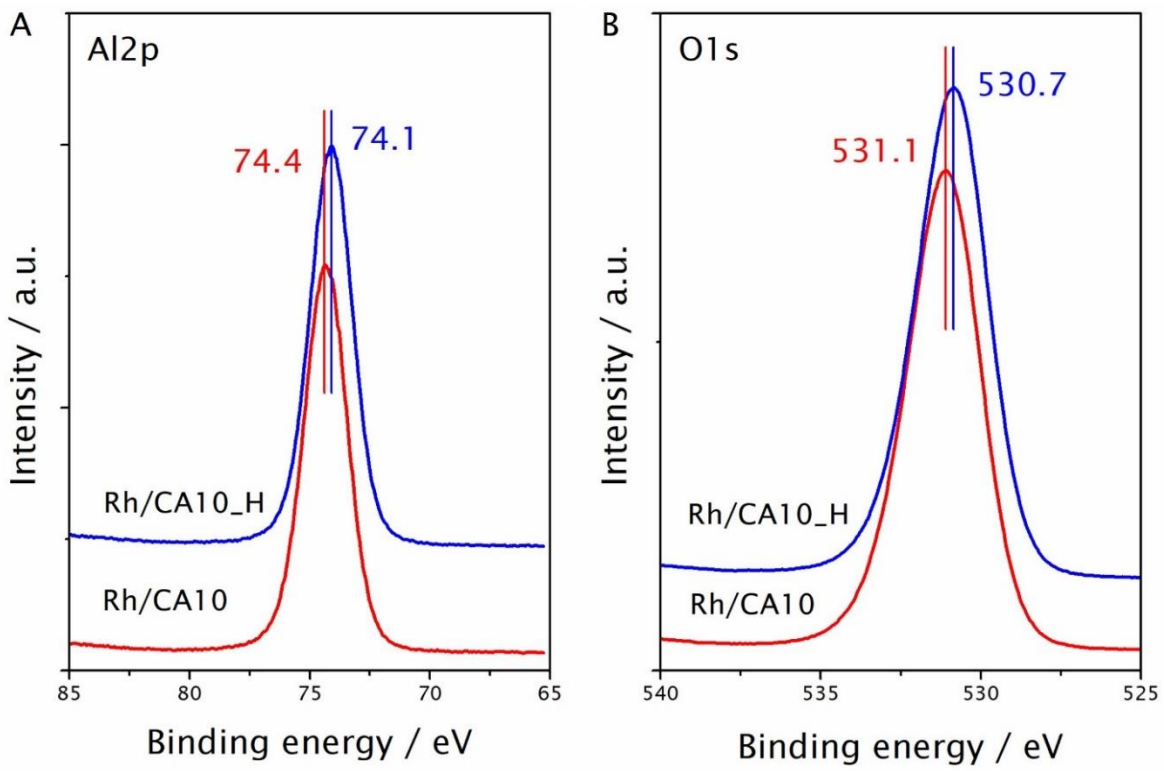

Fig. S18. Al2p (A) and O1s (B) XPS spectra of Rh/CA10 and Rh/CA10_H.

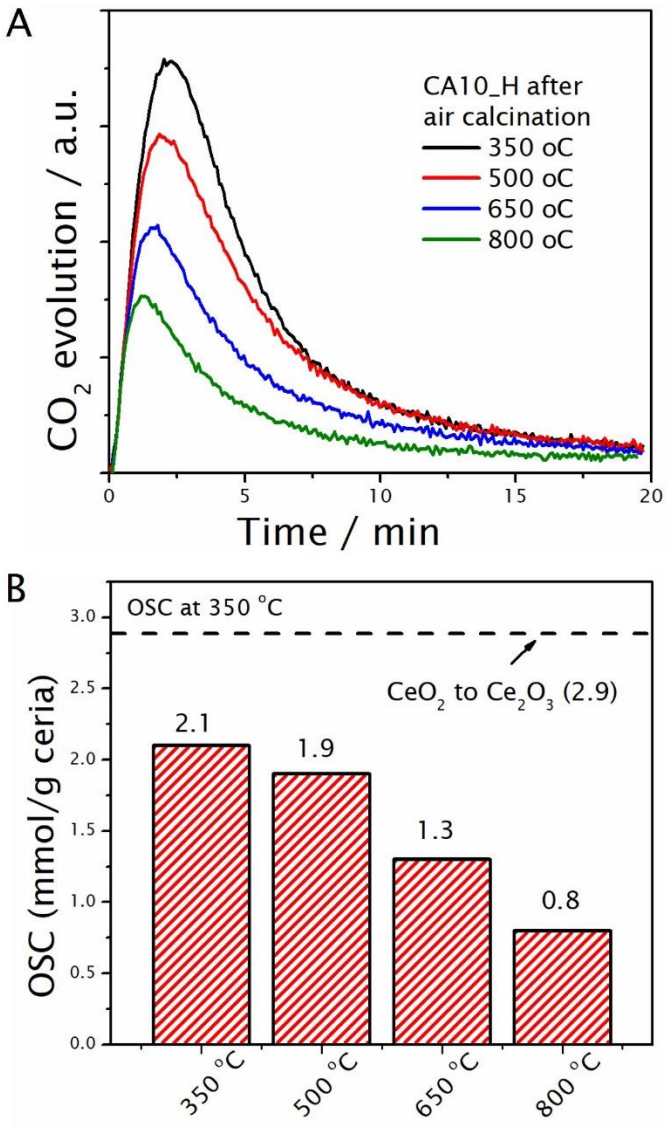

Fig. S19. Oxygen storage capacity (OSC) measurements at 350 ºC on CA10_H after an oxidative pre-calcination at different temperatures from 350 to 800 ºC.

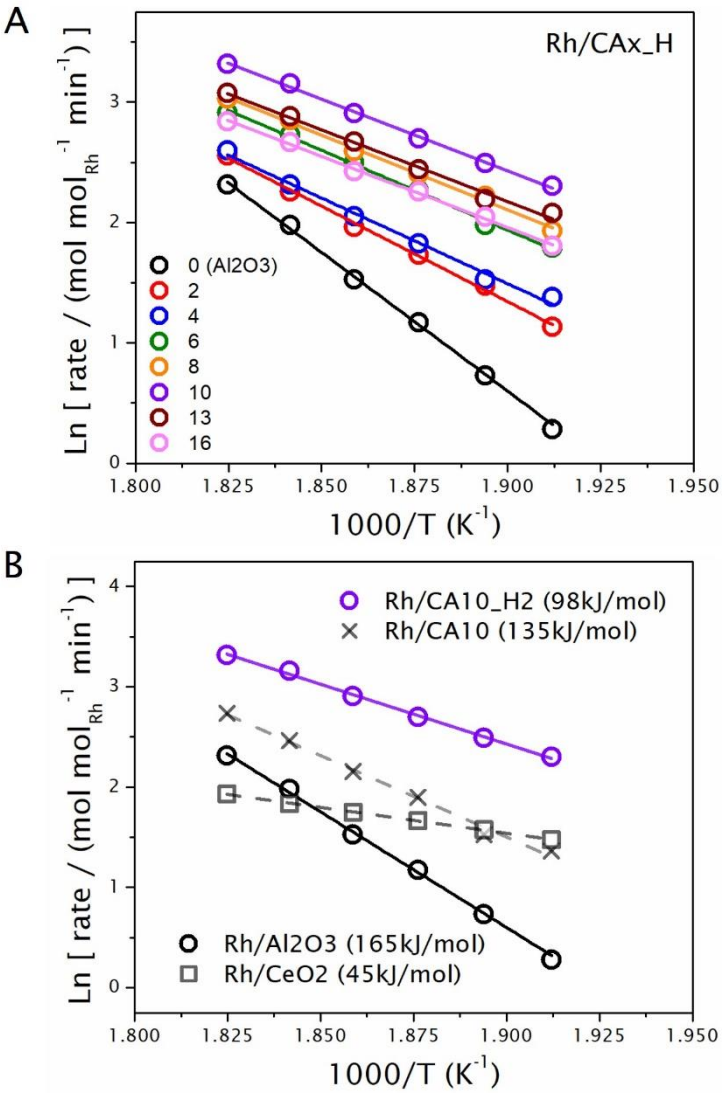

Fig. S20. Reaction rates and apparent activation energies (E_a) of Rh supported on bare Al_2O_3, bare CeO_2, CA10, and a series of CAx_H supports. Reaction steam consisted of 1000 ppm NO and 2000 ppm CO, balanced with N_2. Reaction rates were measured below 10 % NO conversion for all catalysts in the range of 250-275 °C.

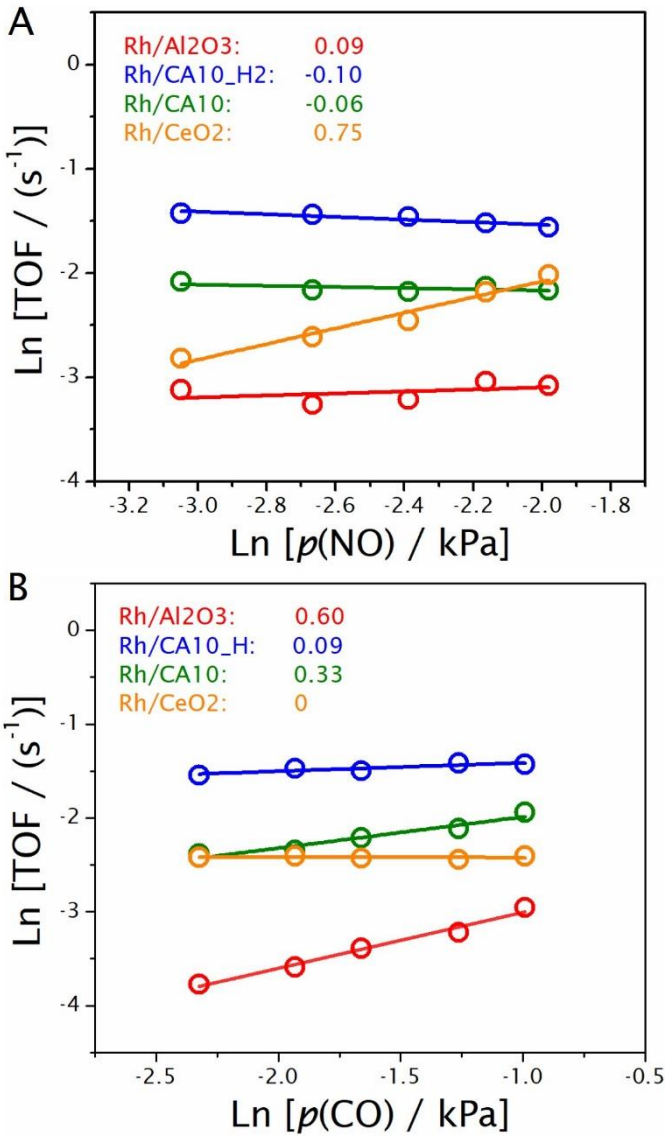

Fig. S21. Reaction rate dependence (reaction orders) on the partial pressures of NO and CO over Rh supported on bare Al_2O_3, bare CeO_2, CA10, and CA10_H. Measurements were conducted at 260 °C below 10 % NO conversion for all catalysts under all the NO/CO partial pressures. NO order was measured in the range of 500-1500 ppm when CO is fixed at 2000 ppm. CO order was measured in the range of 1000-4000 ppm when NO is fixed at 1000 ppm.

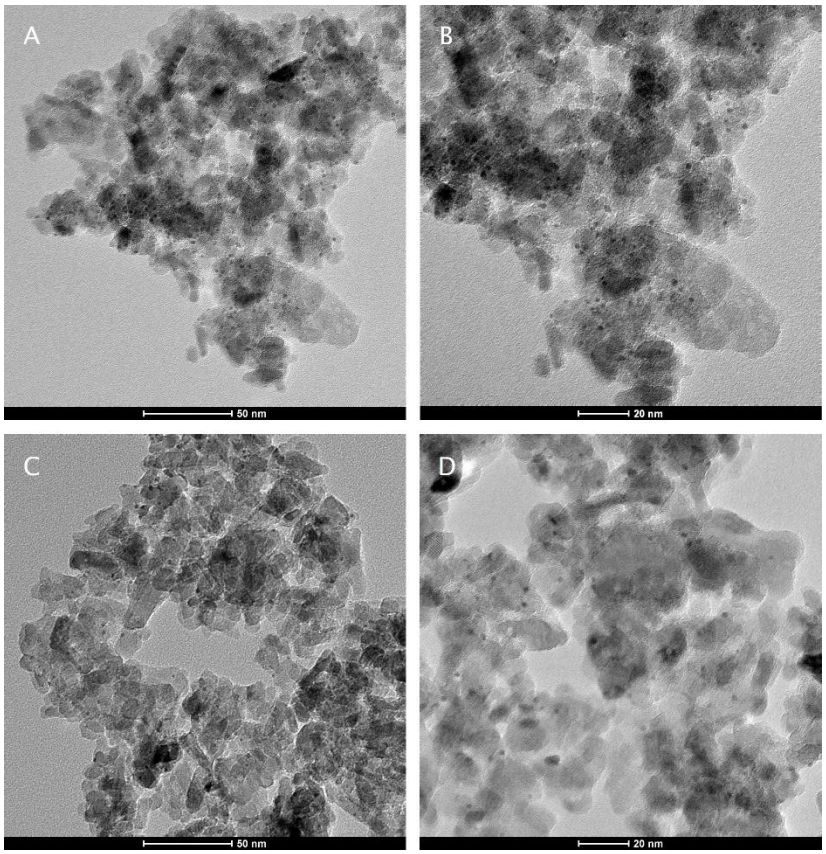

Fig. S22. TEM images of colloidal Pt NPs supported on bare Al_2O_3 (A, B) and CA10 (C, D).

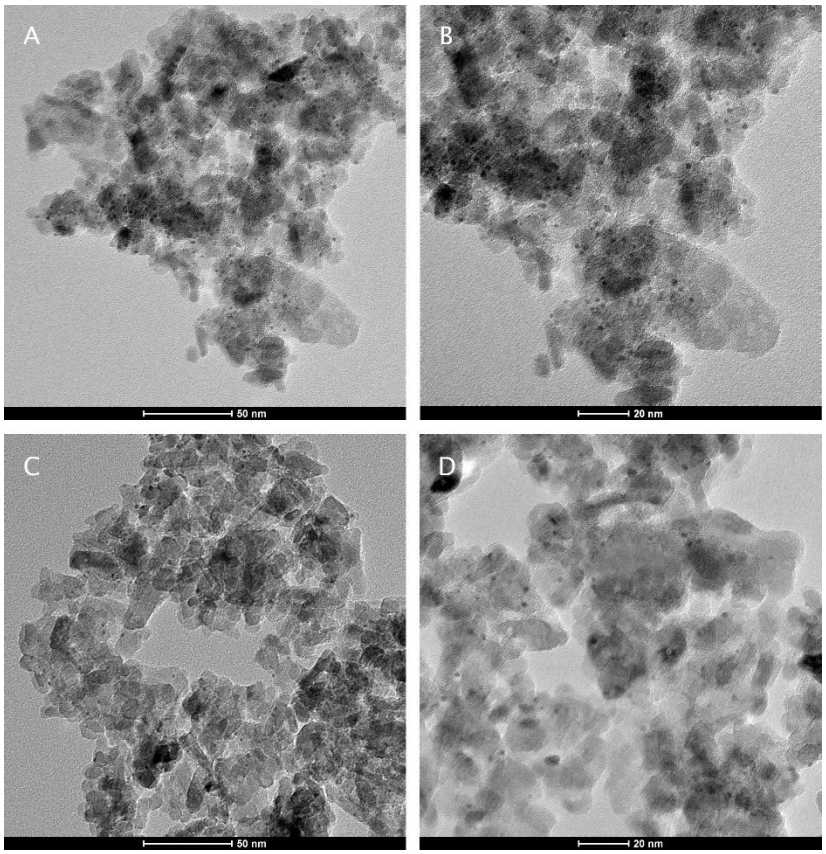

Fig. S23. TEM images of colloidal Pt NPs supported on CA10_H (A, B) and the spent catalyst after lean oxidation of CO and hydrocarbons (C, D). Use of colloidal Pt NPs excludes the interference from difference in nuclearity and particle size when evaluating the impact of different support in the catalytic properties of supported Pt.

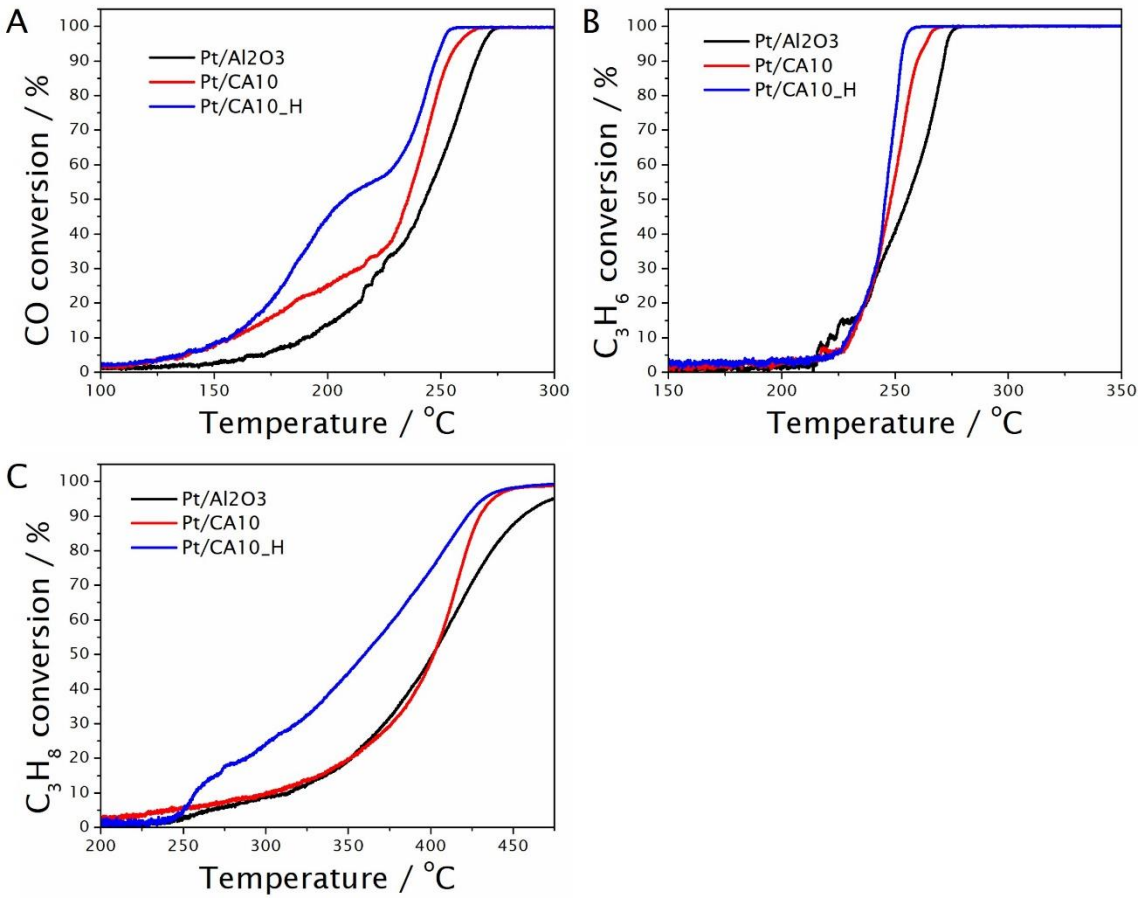

Fig. S24. Light-off performance of Pt/Al_2O_3, Pt/CA10, and Pt/CA10_H catalysts during the lean oxidation of CO (A), C_3H_6 (B), and C_3H_8 (C). Reaction conditions: 0.3 % CO, 0.1 % propane (C_3H_8), 0.1 % propylene (C_3H_6), and 3 % O_2 balanced with N_2 with a total flow of 300 ml min^{-1}. The GHSV is 150,000 ml g^{-1} h^{-1}.

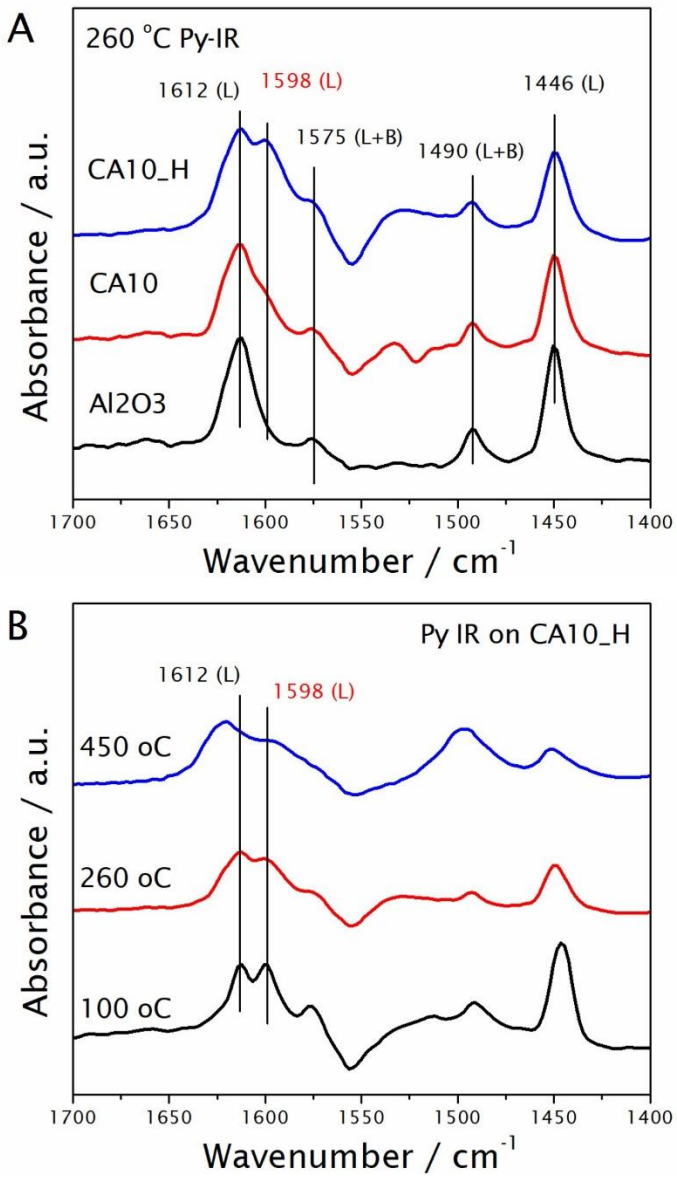

Fig. S25. (A) Pyridine-IR spectra collected at 260 °C over bare Al_2O_3, CA10, and CA10_H after pyridine adsorption and helium purging, clearly showing the presence of a new Lewis acid site on CA10_H. (B) Temperature-programmed pyridine desorption conducted on CA10_H, indicating that the formed 1598 L-acid site is a weaker acid site.

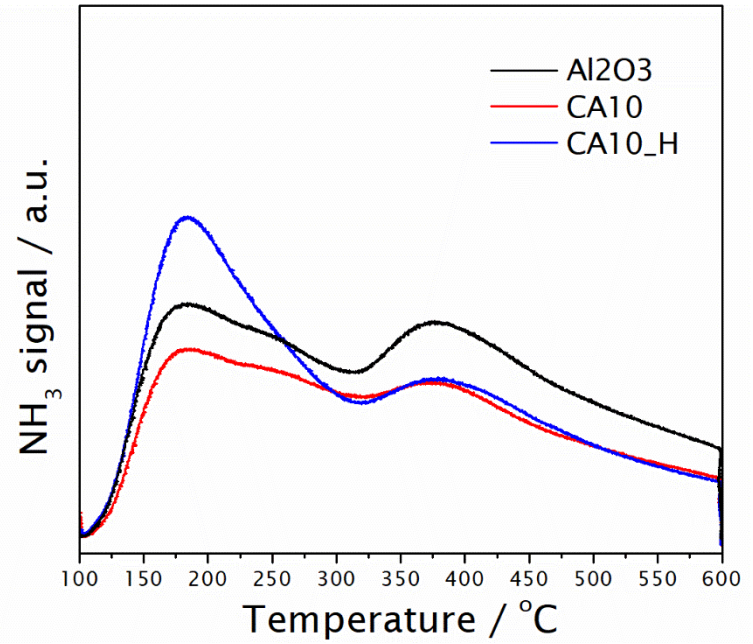

Fig. S26. NH_3 temperature-programmed desorption profiles collected over bare Al_2O_3, CA10, and CA10_H after NH_3 adsorption and helium purging. NH_3 desorption at lower (< 300 °C) and higher (300-600 °C) temperatures comes from NH_3 adsorption on weaker and stronger Lewis acid sites, respectively, also corroborating the 1598 cm^{-1} pyridine IR assignment..

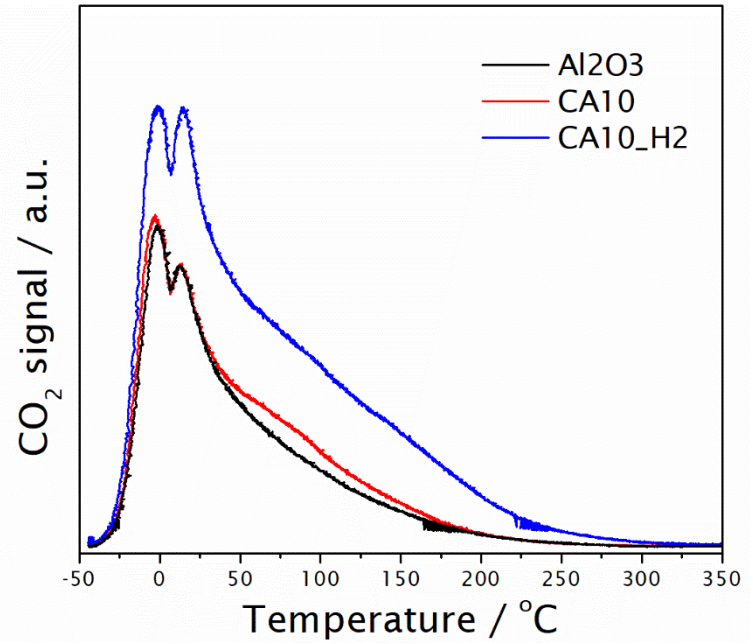

Fig. S27. CO_2 temperature-programmed desorption profiles collected over bare Al_2O_3, CA10, and CA10_H after CO_2 adsorption and helium purging. CO_2 desorption at lower (< 50 °C) and higher (50-250 °C) temperatures can be ascribed to CO_2 adsorption on weaker and stronger Lewis acid sites, respectively.

Table S1. Ce L_{III}-edge EXAFS fitting results of Rh/CA10 and Rh/CA10_H.[a]

Sample	Path	R (Å)	CN	$\sigma^2 \times 10^3$ (Å^2)	ΔE_0 (eV)	R factor
Rh/CA10	Ce-O	2.31 ± 0.02	7.26 ± 1.53	6 ± 4	6.51 ± 1.37	0.052
	Ce-Ce	3.83 ± 0.02	5.78 ± 2.84	0 ± 4	6.51 ± 1.37	
Rh/CA10_H	Ce-O	2.22 ± 0.02	7.74 ± 1.94	19 ± 6	0.72 ± 1.72	0.010
	Ce-Al	2.99 ± 0.04	1.24 ± 1.00	3 ± 10	0.73 ± 1.72	

[a] Please note that the Ce L_{III}-edge is at a relative low energy which is sensitive to the environmental air absorption though the measurement was mostly done under He, and the relatively high error bar is due to the noise at higher k.

References.

36. B. Ravel, M. Newville, ATHENA, ARTEMIS, HEPHAESTUS: data analysis for X-ray absorption spectroscopy using IFEFFIT. *J Synchrotron Radiat* **12**, 537-541 (2005).
37. S. I. Zabinsky, J. J. Rehr, A. Ankudinov, R. C. Albers, M. J. Eller, Multiple-Scattering Calculations of X-Ray-Absorption Spectra. *Physical Review B* **52**, 2995-3009 (1995).
38. N. R. Jaegers, W. Hu, Y. Wang, J. Z. Hu, High-Temperature and High-Pressure In situ Magic Angle Spinning Nuclear Magnetic Resonance Spectroscopy. *J. Vis. Exp.*, (2020).
39. J. Z. Hu *et al.*, High field 27Al MAS NMR and TPD studies of active sites in ethanol dehydration using thermally treated transitional aluminas as catalysts. *Journal of Catalysis* **336**, 85-93 (2016).
40. E. Paparazzo, Use and mis-use of x-ray photoemission spectroscopy Ce3d spectra of Ce2O3 and CeO2. *Journal of Physics: Condensed Matter* **30**, 343003 (2018).